Asteroseismic Study of the Subgiant HD 82074

by

Victoria Ashley Villar

Submitted to the Department of Physics
in partial fulfillment of the requirements for the degree of

Bachelor of Science in Physics

at the

MASSACHUSETTS INSTITUTE OF TECHNOLOGY

June 2014

Signature redacted

Author .....
Department of Physics
May 9, 2014

Signature redacted

Certified by ..
John A. Johnson
Harvard Department of Astronomy
Signature redacted Thesis Supervisor

Certified by ....
Joshua N. Winn
Department of Physics
Thesis Supervisor

Signature redacted

Accepted by .....
Nergis Mavalvala
Senior Thesis Coordinator, Department of Physics

Asteroseismic and Interferometric Study of the Subgiant HD 82074

by

Victoria Ashley Villar

Submitted to the Department of Physics
on May 9, 2014, in partial fulfillment of the
requirements for the degree of
Bachelor of Science in Physics

Abstract

This thesis analyzes HD 82074, a solar-mass and low-metallicity subgiant star, using ground-based asteroseismology with the CHIRON spectrometer at the Cerro Tololo Inter-American Observatory (CTIO) and interferometry with the CHARA array on Mt. Wilson. The physical parameters of subgiant stars are of particular interest in the exoplanetary field due to their importance in understanding the relationships between planet occurrence rate and stellar properties such as age, metallicity and mass. Potential systematic uncertainties in the canonical stellar models make it especially important to independently determine the masses and radii of these stars. We determine HD 82074's radius using interferometry from CHARA, and we combine this result with measurements of the spacing and frequencies of the asteroseismic oscillations of HD 82074 to determine a stellar mass. We find that the star has a radius of 3.96±0.12 solar radii and a mass of 1.20±0.11 solar masses. While the radius is in excellent agreement with predictions from spectral analysis, the mass is 2.9-σ greater than the predicted mass. This suggests that errors of stellar models may be underestimated for low-metallicity or evolved stars. This study makes HD 82074 the third subgiant for which a physical radius is confirmed interferometrically and one of ten asteroseismically studied subgiants.

Thesis Supervisor: John A. Johnson
Title: Professor of Astronomy

Thesis Supervisor: Joshua N. Winn
Title: Associate Professor of Physics

Acknowledgments

Foremost, I would like to express my deepest gratitude to Professor John Johnson and Professor Joshua N. Winn, my research supervisors, for their guidance, patience, support and valuable critiques of this thesis. Being a member of Professor Johnson's research group for the past year has been an incredible learning experience, and I am grateful for the opportunity.

I would also like to thank my collaborators: Professor Debra Fischer, Tabetha Boyajian and Tim White for their advice and contributions to this work. My gratitude is also extended to the SMARTS observing team.

I thank my friends for keeping me grounded and Alex McCarthy for his selfless aid and encouragement.

Finally, I wish to thank my family for their continuous support throughout my entire academic career.

Contents

List of Figures

List of Tables

Chapter 1

Introduction

Today, there are well over one thousand discovered exoplanets and several thousand exoplanet candidates [62]. Exoplanetary systems are diverse and often dissimilar to our own Solar System. Unlike the nearly circular orbits which are aligned with the equator of the sun to within ten degrees, exoplanets have been found to have a range of eccentricities and inclination angles relative to their host star. Additionally, we have discovered Jupiter sized planets whose semi-major axes are only a fraction of the size we see for gas giants in our system. This unexpected range of features has helped drive the exoplanetary field to conduct a wide range of exoplanet surveys in order to understand the distribution and formation of planets and their host stars. With our current sample size, we are just beginning to be able to answer some of these overarching statistical questions.

However, the biases and limitations of our detection methods impede our progress in understanding exoplanetary systems. Each method occupies a distinct sector of exoplanetary parameter space which it can probe under realistic time and resolution constraints, as seen in Figure 1-1. For each technique there are also intrinsic degeneracies between planetary and stellar parameters. In fact, with the exception of direct imaging, all detection methods of exoplanets are indirect measurements relying heavily on the planet's host star.

For example, one of the first and most successful detection methods relies radial velocity measurements. Radial velocity (RV) surveys look for the "wobble" in stars,

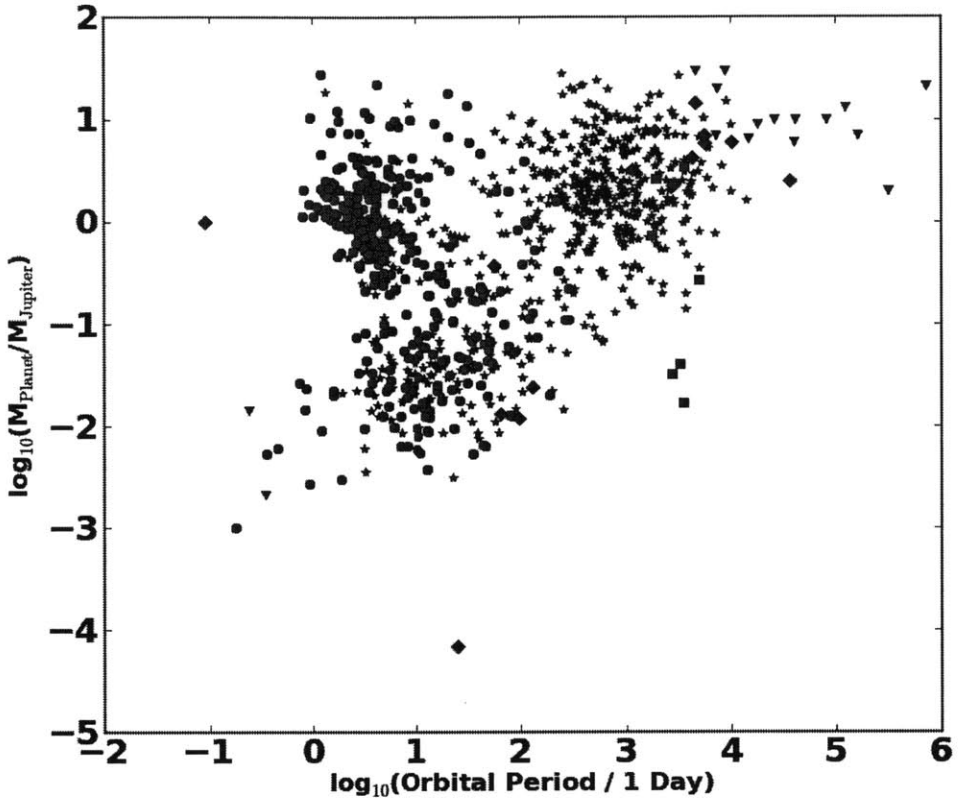

Figure 1-1: Confirmed exoplanets from The Extrasolar Planets Encyclopedia. Five methods of exoplanet detections are shown: radial velocity measurements which are described in the text (blue stars); Transiting planets which uses the dip in stellar light as an exoplanet passes in the line of sight (red circles); Microlensing which searches for abnormalities in typical microlensing events as two stars overlap in our line of sight (black triangles); Timing variations which arise from pulsar signal variations or variations within another exoplanet's orbit. These methods cover distinct ranges of parameter space for exoplanets.

or changes in the star's velocity in the observer's line of sight. For a star hosting an exoplanet, the amplitude (K) of the observed radial velocity of the star is given by:

$$K = \frac{2\pi a_* \sin(i)}{P\sqrt{1-e^2}} \tag{1.1}$$

where a_* is the semimajor axis of the stellar orbit, i is the inclination angle of the planet and P is the period of the planet. The inclination angle is defined such that

$i = 0^o$ when the orbit of the planet is perpendicular to the observer's line of sight ("face-on"), and $i = 90^o$ when the orbit of the planet is parallel to the observer's line of sight ("edge-on"). This relationship can be combined with Kepler's third law, $P^2 = \frac{4\pi^2}{G(M_* + M_p)} a_p^3$, to provide the simple relationship:

$$\begin{aligned} K &= \left(\frac{2\pi G}{P}\right)^{1/3} \frac{M_p \sin(i)}{(M_* + M_P)^{2/3}} \frac{1}{\sqrt{1-e^2}} \\ &\simeq 28.5[\mathrm{ms}^{-1}] \left(\frac{P}{1\ \mathrm{yr}}\right)^{-1/3} \left(\frac{M_p}{M_{\mathrm{Jup}}}\right) \left(\frac{M_*}{M_\odot}\right)^{-2/3} \left(\frac{\sin(i)}{\sqrt{1-e^2}}\right) \end{aligned} \tag{1.2}$$

It is clear that radial velocity measurements tend to detect more massive planets with edge-on orbits around lower mass stars. Indeed, this fact has guided RV surveys to focus on lower mass FGK dwarfs as seen in Figure 1-1. It is also evident that for any given K measurement there is degeneracy amongst the parameters in Equation 1.2. While the period and eccentricity can generally be detangled from the RV time series, there is a lingering degeneracy between the mass of the planet and the mass of the host star. Either another detection method must be used (with its own set of limitations), or an independent estimate of the star's mass is necessary to break the degeneracy.

In addition to better understanding the planets themselves, characterization of the stars can help answer questions about the environments in which exoplanets form. For massive gas giants (such as the hot Jupiters typically detected by RV studies), there are two widely supported theories: core accretion and disk instability [47, 8]. Core accretion predicts that planet formation begins with the coagulation of particles and collision of planetesimals until the planet core reaches a critical mass of 10-20 Earth masses. At this mass, the core rapidly accretes gas from the surrounding protoplanetary disk material. The core accretion theory predicts an increase in planet abundance with stellar metallicity and mass due to shorter accretion timescales and broader formation regions within the disk, respectively [13, 31, 36, 55].

In contrast to this bottom-up approach, the disk instability model predicts that gas giants form as the massive, unstable protoplanetary disk rapidly cools and fragments [31]. Disk instability predicts no dependence of planet formation on stellar properties,

including mass and metallicity [10, 9]. Notably, the independence between stellar mass and planet abundance is due to the short lifetime of the planet formation ($\sim 10^3$ yrs) versus the lifetime of the disk ($\leq$ 3 Myr) for low mass stars. This timescale discrepancy correctly predicts the possibility of giant mass planets around M dwarfs and naturally predicts planets around more massive stars [10].

The evolution of planetary systems can also be understood through studies of host stars. Any planetary formation and evolution theory must explain the great diversity seen in exoplanetary systems across every stage of the host stars life. In general, larger planets are expected to form beyond the ice line of a star, where more solid grains are available for accretion. However, as previously stated, Jovian planets can be seen well within one AU of the host star. To account for this discrepancy, theories invoke migration mechanisms of planets within the protoplanetary disk. Giant planets which are sufficiently close to their host star after migration are expected to spiral closer to their host stars via tidal transfer of angular momentum [45]. The effects of stellar evolution and interaction on these planetary dynamics are uncertain.

Recent Doppler surveys show a positive correlation between stellar mass (and metallicity) and planet abundance, with a deficit in giant planets with periods on the order of days around massive stars ($\geq$1.3 solar masses). These results are from RV surveys of M dwarfs, FGK dwarfs and evolved subgiants known as "retired A stars" [33, 31]. These results support the core accretion model. Additionally, the paucity of massive stars with short-period, massive planets suggest that protoplanetary disks of massive stars may inhibit the formation of such planets. Because the RV method is biased towards the detection of massive, closer-in planets, the apparent gap in short-period planets is not an effect of observational bias [32].

These important results rely on spectroscopic measurements of the aforementioned "retired A stars", or evolved subgiants. Subgiants are stars which brighter than dwarf stars yet dimmer than giant stars. They are stars ending the process of hydrogen fusion within their cores, but have not yet ascended the red giant branch. Subgiants make excellent RV targets because they are cooler and rotate more slowly than their main sequence counterparts. This both increases and narrows the observable absorp-

tion lines within their spectra [23]. While main sequence A star's broadening and velocity 'jitter' which limits Doppler precision to 90-200 m s^{-1}, retired A stars have internal noise on the order of 5 m s^{-1} [63, 25].

However, the measured properties of "retired A stars" may suffer from systematic error and large uncertainties which were unaccounted for. This is partially due to crossings of stellar evolutionary tracks along the Hertzsprung-Russell (HR) diagram. The HR diagram is a plot of brightness versus spectral type for many stars. Because these properties change as a function of time, metallicity and density, HR diagrams are often used to determine the basic physical properties of stars. This is a straightforward process for main sequence stars, but the evolutionary tracks of subgiants with masses between one and two solar masses cross over one another. This can be seen in Figure 1-2. Uncertainties are also unaccounted for in the assumptions made by the stellar models. Notably, the mixing length (the characteristic length a cell of material will move within a star), is set based on solar observations. However, the assumption that the mixing length should be constant across the HR diagram is not well tested [49]. The difference between a $1.3M_{\odot}$subgiant and a $1.7M_{\odot}$subgiant is only a difference on 200K in T_{eff} and 0.2 dex in [Fe/H], acquired by a change of 5% in mixing length.

Additional systematic errors may exist within the analysis method itself. The spectral analysis method, Spectroscopy Made Easy (SME), which is used in these studies has known systematic errors (Valenti & Fisher 2005) [42]. For example, Torres et al. (2008) found correlations between T_{eff} and [Fe/H] in SME, and systematic differences in T_{eff} and metallicity between SME and line-by-line spectral analysis which can lead to systematic mass-estimate errors as large as 15% for sun-like stars. This can be corrected by forcing the spectroscopic surface gravity to match the model-predicted surface gravity, but the correction intrinsically assumes that the model grids are accurate [57]. The uncertainties of the analysis for cooler, less dense stars like subgiants are not well studied.

Based on these arguments and a expected observational bias towards lower mass stars due to their lifespan on the subgiant branch, Lloyd (2011,2013) concludes that these "retired A stars" may in fact be a population of evolved F- or G-type stars,

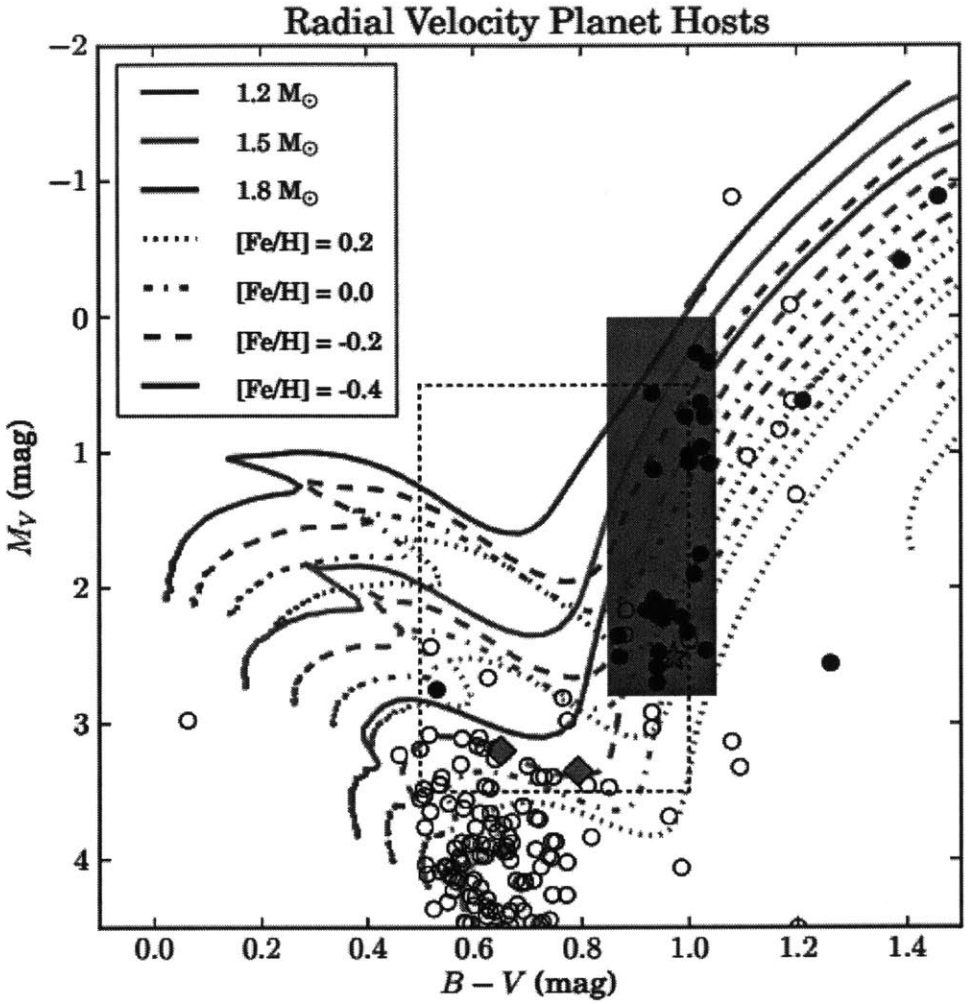

Figure 1-2: HR diagram showing B-V color versus absolute V magnitude of host stars with planets found before May 2011. Hosts with $M_* > 1.5M_\odot$are shown in filled circles, while hosts with $M_* < 1.5M_\odot$are shown in open circles. The dotted-line box shows the parameter space of the sample of evolved stars in Johnson et al. (2006) ($0.5 < M_V < 3.5$; $0.5 <$ B-V < 1.0). The shaded region contains 28 hosts with $M_* > 1.5M_\odot$and 3 with $M_* < 1.5M_\odot$. The lines are evolutionary tracks of hosts of 1.2, 1.5 and $1.8M_\odot$ranging in metallicity from -0.4 to 0.2. These tracks were derived from Yonsei-Yale isochrones. Figure taken from Lloyd (2011) [42, 64].

with masses closer to a solar mass. While it is uncertain whether the lifespan of G- versus A- type subgiants has a significant effect the RV survey results, the previous arguments do indicate a discrepancy that might arise from misidentifying the true population of "retired A stars" [30].

This theory was independently tested by Schlaufman & Winn (2013), using the stellar velocity dispersion of the subgiant population in question[52]. All stars form through highly dissipative, dense gases which create relatively a low velocity distribution in the stellar population at the time of creation. For older stars, the velocity dispersion of older generation stars tends to be higher. This is due to interactions between the stars and the surrounding molecular gas, as well as density perturbations within the spiral-disk of the galaxy [5]. Because massive star's have a higher rate of nuclear fusion, they spend less time on the main sequence. Therefore, higher mass stars in the subgiant stage are typically younger than their lower mass counterparts. In turn, this implies that massive (A-type) star populations should have less velocity dispersion relative to the less massive populations (F- and G-types) [52]. This test revealed that the velocity dispersion of the "retired A stars" is consistent with that of F5- to G5-type stars and inconsistent with that of A5- to F0-type stars.

The true class of these stars can reveal whether their population of planets is simply a dynamic consequence of their age or characteristic of massive host stars in general. If the retired A stars have over-estimated masses, the lack of short period planets around the subgiants may indicate that tidal capture during the evolution of the star plays a large role in planetary dynamics. Moreover, the increased planet frequency in these subgiants compared to main-sequence F- and G- dwarfs may point to a systematic flaw in the measured metallicities [42].

Rather than relying on evolutionary models or indirect measurements, stellar masses can be accurately measured using asteroseismology. Asteroseismology is the study of stellar oscillations caused by pressure and temperature perturbations which are often excited through convection. In short, acoustic waves are refracted towards the star's cooler surface, where they are reflected against the star's outer boundary, or the photosphere. The reflections are again refracted and reflected, creating a periodic signal on the stars surface. The signal can be used to determine the density, surface gravity and age of the star [1, 29]. s This asteroseismic signal is detected using RV measurements or photometry. For subgiants and giants, the expected RV signal for the lower order modes is on the order of 1 m/s. This resolution has become possible

from terrestrial telescopes within the last two decades due to vast improvements in spectrographs. The expected dominant frequency is on the order of several hours, while the decoherence time of these modes is on the order of days [28, 6]. Photometric measurements of subgiants can also be made with high precision instruments capable of detecting flux variations on the order of 20 parts per million.

In this thesis, we will explore the possibilities of asteroseismology in evolved stars. Specifically, we will study HD 80274, a G-type subgiant. In Chapter II we will give the theoretical background of the source of these oscillations. In Chapter III we will present our observational strategy and observations using CHIRON for the subgiant HD 82074. In Chapter IV we will present our interferometric measurements of radius for HD 82074. In Chapter V we will present the methods for studying these mechanisms, and we will summarize the results in Chapter VI.

Chapter 2

Theoretical Background

Asteroseismology is the study of subsurface oscillation within stars. The understanding of these oscillations modes can lead to a general insight of stellar interiors by tracing the eternal battle between internal excitations of the star and its fundamental restoration forces.

2.1 Excitation and Restoration Processes

Stellar modes are typically excited by either stochastic processes or the κ mechanism. Stochastic processes arise from convection in the upper layers of the star. The large temperature gradient in this area leads to near-sonic to super-sonic, turbulent motion of material. This turbulent noise excites the observable eigenmodes of star. The modes have a characteristic lifetime in which the mode dampens and the phases decorrelate. Stochastic processes occur in main sequence stars less than $2M_{\odot}$and evolved stars which are cooler than the instability strip [54, 50].

The κ mechanism is a pseudo-periodic process in which shell of material is perturbed and moves radially to maintain equilibrium. This radial movement causes a change in the opacity (or temperature) within the shell. For example, a shell of He I may drift deeper within the star and compress and ionize to He II. The local opacity, or the ability for electromagnetic radiation to pass through the region, raises as He I ionizes. Trapped heat raises local pressure. The shell then expands, cools and allows

recombination to occur. As the shell cools it begins to contract once again and repeat the cycle. This process mainly occurs within the instability strip of the HR diagram, such as Cepheid variables and δ Scuti stars.

Rarer sources of variability are the ϵ mechanism and convective blocking. In the ϵ mechanism, the stars core heats due to a short-term acceleration in nuclear reaction rate, causing the nearest material to expand, cool and again shrink. This mechanism may excite g modes in δ Scuti variables and Wolf-Rayet stars [41, 7]. Convective blocking occurs when perturbations arise in the transitional region between the convective and radiative zones of the stars, but the convection rate is too slow to transport this energy efficiently, leading to driven pulsations.

These modes are further classified by their restoration forces: pressure (p modes), buoyancy (g modes) and surface gravity (f modes). The distinction between these classes is formalized by defining the buoyancy (or Brunt-Väisälä) frequency (N) and the acoustic frequency (S_l). While both frequencies scale with the square-root of the average density of the star, N scales linearly with the surface gravity, and S_l scales linearly with the sound speed. P modes have angular frequencies (ω) greater than N and S_l, while g modes have angular frequencies less than N and S_l. F modes exist only on the surfaces of stars, so this classification does not apply. Each type (p, g and f modes) are associated with a unique physical phenomenon:

p modes: Longitudinal density waves in convective zones cause p modes. The properties of p modes are defined by the local sound speed, which primarily depends on pressure and temperature. They are essentially radial modes trapped in a cavity formed by the stars sharp outer layer and rapidly increasing density and temperature gradients near the core. The gradients cause the wave to bend according to Snell's law as they encounter higher sound speeds near the core. The depth to which these waves can penetrate depends on the order (n) of the waves, which will be defined in the next section.

g modes: Gravitational or buoyancy forces drive g modes in stars. Radial motion of matter across the density gradient drives corrective buoyant forces. G modes are confined to the radiative zones of stars where their frequencies will be less than the

Brunt-Väisälä frequency. Because evolved stars tend to have outer radiative zones, g modes are visible in mainly evolved stars and are not well studied within our own sun. P modes and g modes can overlap in evolved stars where the radiative region is large; this phenomenon is called a mixed-mode. Figure 2-1 shows the propagation of p and g modes in a Sun-like star [4].

f-modes: F modes occur on the surface of stars or on the boundary between convective and radiative zones. These modes have the same restorative force as g modes: buoyancy. However, f modes are surface gravity waves which have no radial nodes and approximately no radial dependence. F modes are appropriately described as short surface gravity waves in the "deep water" limit, or in the limit at which the distance to the absolute lower boundary is much less than the amplitude of the waves themselves [44].

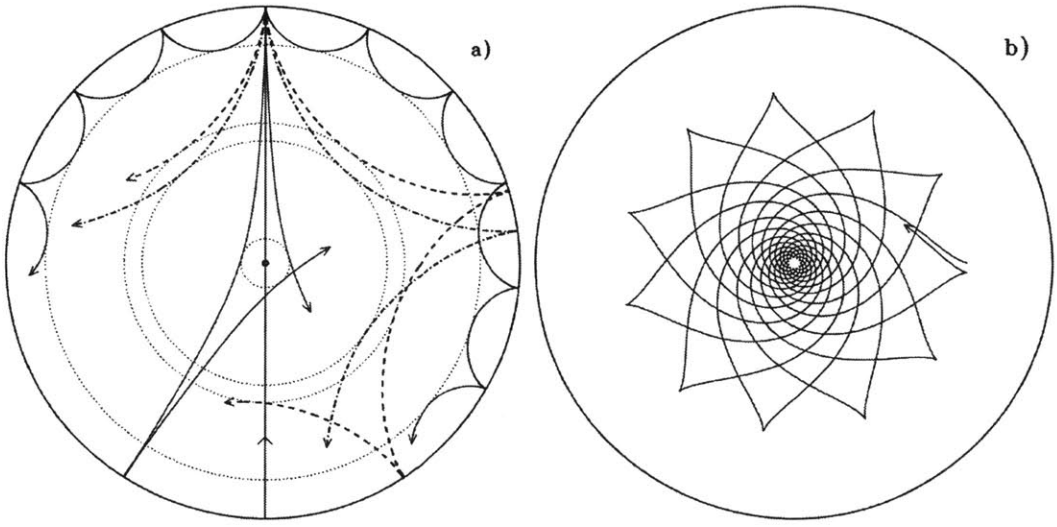

Figure 2-1: Propagation of acoustic and gravity waves in a Sun-like star. Panel (a) demonstrates how the p mode paths bend radially outwards with increasing depth, until reaching their various inner turning points" and undergoing total internal refraction. Panel (b) traces a g mode ray path which is trapped in the inner radiative layer of the star. The ray path of the g modes depend heavily on the star's core conditions [22, 2]. Figure taken from Aerts et al. (1996).

2.2 Spherical Harmonics

Approximating the star as spherically symmetric, the various oscillations can be described mathematically in the (r,θ,ϕ) coordinate system, where r is the distance from the center of the star, θ is the colatitude and ϕ is the longitude. The oscillatory modes solve the spherical wave equation:

$$\Delta^2 \xi = \frac{1}{c(r)^2} \frac{\partial^2 \xi}{\partial^2 t^2} \tag{2.1}$$

which can be written as:

$$\xi_r(r,\theta,\phi,t) = a(r) Y_l^m(\theta,\phi) \exp(-i2\pi\nu t) \tag{2.2a}$$

$$\xi_\theta(r,\theta,\phi,t) = b(r) \frac{\partial Y_l^m(\theta,\phi)}{\partial\theta} \exp(-i2\pi\nu t) \tag{2.2b}$$

$$\xi_\phi(r,\theta,\phi,t) = \frac{b(r)}{\sin\theta} \frac{\partial Y_l^m(\theta,\phi)}{\partial\theta} \exp(-i2\pi\nu t) \tag{2.2c}$$

where ξ_r, ξ_θ and ξ_θ are displacements of matter, $a(r)$ and $b(r)$ are amplitudes of the displacement which encode $c(r)$, ν is the frequency and $Y_l^m(\theta,\phi)$ are spherical harmonics. Given a $c(r)$, these solutions are completely specified by three numbers:

1. n, the overtone of the mode
2. l, the degree of the mode which specifies the number of surface nodes present.
3. m, the azimuthal order whose absolute value specifies how many surface nodes are lines of longitude. The azimuthal order can range from l to -l.

Sample harmonics are shown in Figure 2-2 and the typical frequencies and degrees l of the modes is shown in Figure 2-3.

2.3 Asymptotic and Scaling Relations

For low-order p modes, the inner turning point for modes (in which wave experiences total internal refraction) becomes very close to the core of the star. This implies that

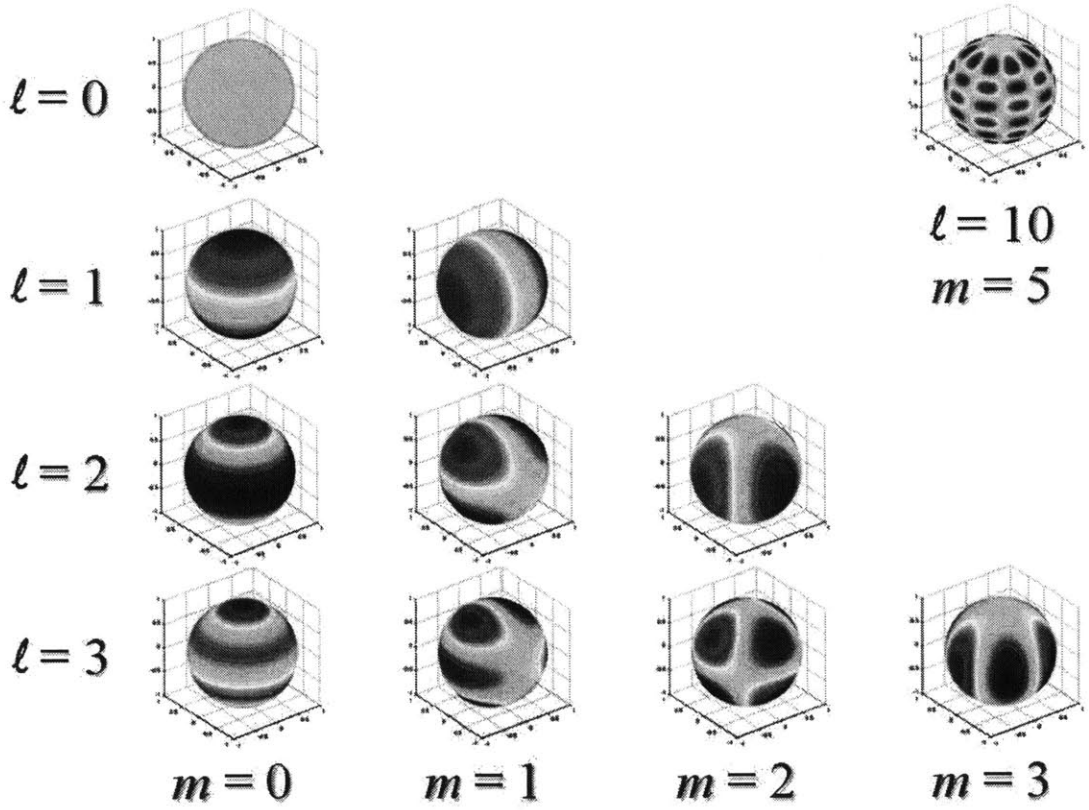

Figure 2-2: Sample spherical harmonics, $Y_l^m(\theta, \phi)$. Blue represents a positive pertubation while red reresents a negative perturbation. Image taken from Ahern (2009) [3].

the path length that low order p modes travel is approximately constant. For large n, the radial spacing of the nodes become approximately equidistant, and perturbations in the gravitational essentially cancel due to the rapid variation. Neglecting the effect of the change in gravitational field as a function of radius is known as the Cowling approximation [21]. The Cowling approximation has proven to be in good agreement with polytropic models and solar observations [15, 60, 16].

Assuming $n \gg 1$ and using the Cowling approximation, we can relate ξ_r, N and S_l:

$$\frac{\mathrm{d}^2\xi_r}{\mathrm{d}r^2} = \frac{\omega^2}{c(r)^2}\Big(1 - \frac{N^2}{\omega^2}\Big)\Big(\frac{S_l^2}{\omega^2} - 1\Big)\xi_r \equiv K_s(r)\xi_r \tag{2.3}$$

For positive K_s, ξ_r has an oscillatory solution, $\xi_r \sim \cos(\int K_s^{1/2} dr + \phi)$. P modes

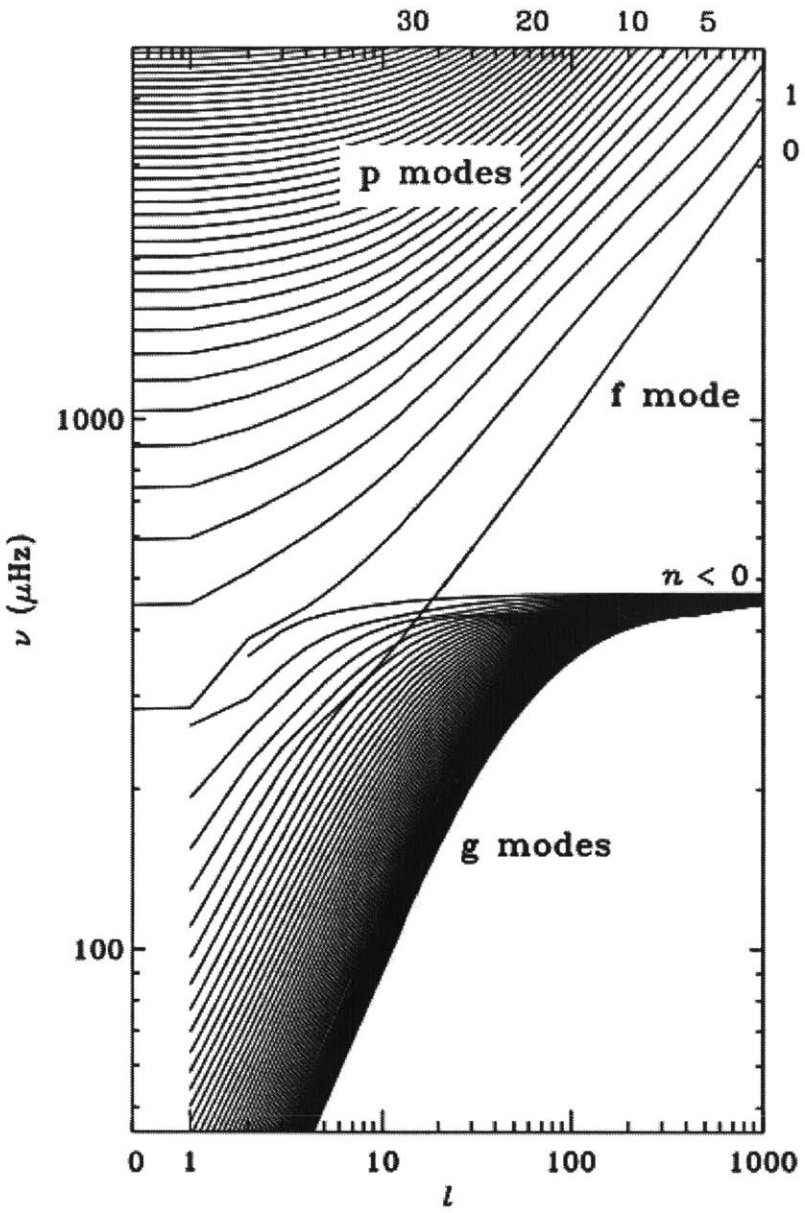

Figure 2-3: Frequency of modes versus their degree l for a Sun-like star. In the upper right corner, a few corresponding overtones (n) are listed for reference. The overtones for the g modes are negative by convention. Solid lines, rather than discrete modes, are used for clarity. The figure illustrates that p modes increase in frequency with increasing overtone and degree, while g modes decrease with overtone but increase with degree. A single f mode is seen crossing the phase space of both g and p modes. Figure from Aerts et al 2010 [19].

with large n have frequencies which are much greater than N. In this regime, $K_s \simeq \frac{1}{c(r)^2}(\omega^2 - S_l^2)$. When we plug in the definition of S_l and divide by ω, this leads to Durvall's law [24]:

$$\omega \int_{r_t}^{R} \left(1 - \frac{L^2 c^2}{\omega^2 r^2}\right)^{1/2} \frac{dr}{c} \tag{2.4}$$

Where $L = l + \frac{1}{2}$ and r_t is the inner turning radius defined such that $\frac{c(r)_t}{r_t} = \frac{\omega}{L}$ [27, 16].

Again, for large n and low degree modes, r_t is close to the center of the star ($r_t \equiv \frac{c(r)L}{\omega} \simeq 0$), and therefore the second term of the integrand is typically much small than unity. Using this fact, we can take a second order approximation and find that:

$$\nu_{n,l} = \Delta\nu(n + \frac{l}{2} + \epsilon) + D_0 \tag{2.5}$$

where ϵ is a constant reltated to the polytropic index of the star. The polytropic index roughly describes the overall density distribution of the star, although ϵ is particular sensitive to surface conditions. For a sun-like star, we expectd $\epsilon \sim 1.4$ and for a fully convective star (such as a red giant) we expect $\epsilon \sim 0.7$. A more precise definition of ϵ can be found in Christensen-Dalsgaard & Hernandez (1992) [18].

$\Delta\nu$ is the large separation and is the inverse of the sound travel time for a wave to propagate from the surface of the star to the core and back:

$$\Delta\nu = \left(2\int_0^R \frac{dr}{c(r)}\right)^{-1} = \nu_{n,l} - \nu_{n-1,l} \tag{2.6}$$

where $c(r)$ is the sound speed and R is the stellar radius. D_0 is a small correction related to the age of the star through the small separation $\delta\nu$, defined as

$$\delta\nu_{n,l} = \nu_{n,l} - \nu_{n-1,l+2} \tag{2.7}$$

Under this second order expansion, D_0 is defined as $\frac{l(l+1)}{(4l+6)}\delta\nu_{0,2}$,

A similar expansion can be performed in the limit that $\omega^2 \ll S_l^2$, corresponding

g modes. In contrast to p modes, the period of g modes are asymptotically approximated by:

$$\Pi_{nl} = \frac{\Pi_0}{\sqrt{l(l+1)}}(n+\epsilon) \tag{2.8}$$

Here, ϵ is a small correcting constant and Π_o is equal to:

$$\Pi_0 = 2\pi^2\Big(\int \frac{N}{r}dr\Big)^{-1} \tag{2.9}$$

Using these relations and basic physics, we can relate the asteroseismic observables with intrinsic properties of the stars. For example, the adiabatic sound speed is the speed of sound within the star when the equation of state can be described by $p \propto \rho^\gamma$, where p is the pressure and γ is the adiabatic index. Assuming the ideal gas law and the adiabatic approximation hold, the speed of sound c is proportional to $\sqrt{\langle T \rangle}$, the average temperature. Using dimensional analysis and Equation 2.6, we see that $\Delta\nu$ should scale as $\frac{\sqrt{\langle T \rangle}}{R_*}$. Pressure can be approximated as the gravitational force of the star overs its area. Using the ideal gas law and the pressure scaling approximation, we find that $\langle T \rangle \propto M/R$. Thus, $\Delta\nu \propto (M/R^3)^{1/2} \propto \sqrt{\rho}$ [37]. Scaling to the density of our sun:

$$\Delta\nu = \left(\frac{\rho_*}{\rho_\odot}\right)^{1/2} \mu Hz \tag{2.10}$$

Likewise, the frequency of the mode with maximum power ($\nu_{\max}$) should scale with the acoustic cutoff frequency of the star (ν_{ac}). The cutoff frequency is defined by the dynamical timescale of the atmosphere and scales as c_s/H_p, where H_p is the pressure scale height of the atmosphere. Frequencies above this cutoff are able to propogate directly through the stellar atmosphere. Here $H_p \propto T/g$, where g is the surface gravity of the star (GM_*/R_*^2) [40]. Assuming an adiabatic sound speed, we find that $\nu_{\max} \propto g/\sqrt{T}$. We can once again scale to the sun :

$$\nu_{\max} = \left(\frac{g_*}{g_\odot}\right)\left(\frac{T_{\text{eff}}}{5777K}\right)^{-1/2} \mu Hz \tag{2.11}$$

Using Equations 2.10 and 2.11, we can directly calculate R_* and M_* from the

observables $\nu_{\max}$ and $\Delta\nu$ and by plugging in solar properties:

$$R = (7.84 \times 10^{-2}) \frac{\nu_{\max} T_{\text{eff}}^{1/2}}{\Delta\nu^2} \mathrm{R}_\odot \tag{2.12a}$$

$$M = (2.66 \times 10^{-8}) \frac{\nu_{\max}^3 T_{\text{eff}}^{3/2}}{\Delta\nu^4} \mathrm{M}_\odot \tag{2.12b}$$

Additional empirical relations have been determined for the expected amplitude velocity of the largest mode (v_{osc}) and the overtone of the maximum-power frequency ($n_{\max}$) [38, 20]:

$$v_{osc} = \frac{L/L_\odot}{M/M_\odot} (23.4 \pm 1.4) \text{ cms}^{-1} \tag{2.13a}$$

$$n_{\max} \simeq 22.6 \left(\frac{M/M_\odot}{(T_{\text{eff}}/5777K)(R/R_\odot)} \right)^{1/2} - 1.6 \tag{2.13b}$$

Because these relations are so simplistic, they have been used to create "asteroseismic Hertzsprung-Russell (HR) Diagrams", which typically plot a function of $\Delta\nu$, $\nu_{\max}$ and effective Temperature. An example can be seen in Figure 2-4. These tools are becoming increasingly important as the astronomical community begins to streamline asteroseismic techniques as a method for understanding planets' host stars.

2.4 Theoretical Spectra

Only a fraction of the theoretically infinite number of eigenmodes described can be excited. For p modes, the natural lower frequency limit comes from the fundamental radial mode, or the single oscillation between the core and the surface of the star. The natural upper limit is the aforementioned acoustic cutoff frequency.

Additionally, there exists an intuitive observational bias for lower degree modes due to the partial cancellation of higher order modes when the observer integrates radial movement over the full surface of the star. This can be quantified by integrating the expected RV response (or intensity response) of the star over its solid angle. Explicitely, the spatial response function for radial velocity is:

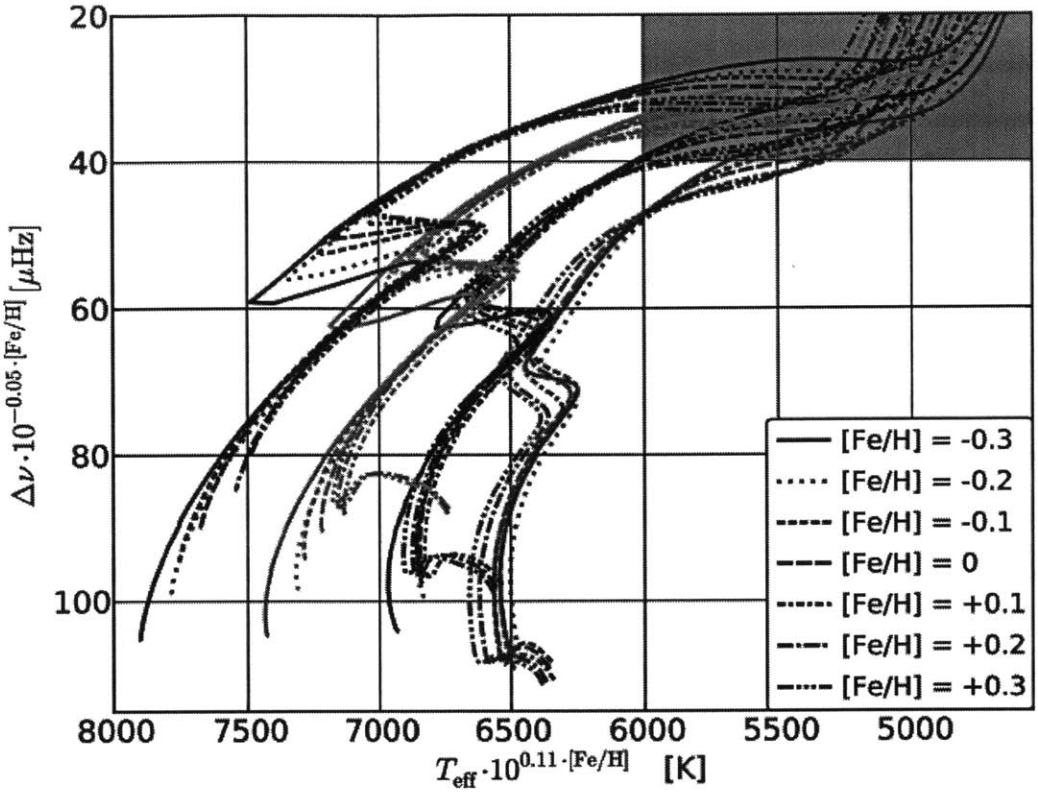

Figure 2-4: Example of an asteroseismic "HR" diagram. Here, a function of effective Temperature T_{eff} is plotted against a function of $\Delta\nu$ and metalliciy [Fe/H]. The colored tracks represent masses ranging from $1.3M_{\odot}$(in magenta) to $1.6M_{\odot}$(blue) in steps of $0.1M_{\odot}$. The line types represent different metallicities, shown in the legend. The tracks beging to overlap in the shaded grey region. Figure taken from Lundkvist et al. (2014) [43].

$$S_l(RV) = 2\sqrt{2l+1}\int_0^{\frac{\pi}{2}} W(\theta)P_l^{|m|}(\cos(\theta))\cos(\theta)^2\sin(\theta)d\theta \tag{2.14}$$

where $P_l^{|m|}(\cos(\theta))$ is the m^{th} order Legendre polynomial which arises from taking the real part of the spatial harmonics $Y_{l,m}$. $W(\theta)$ is a limb-darkening function. The spatial response function for intensity takes a similar form, dropping a factor of $\cos(\theta)$ which arises in the RV equations due to the projection in the observer's line of sight:

$$S_l(I) = 2\sqrt{2l+1}\int_0^{\frac{\pi}{2}} W(\theta)P_l^{|m|}(\cos(\theta))\cos(\theta)\sin(\theta)d\theta \tag{2.15}$$

The expected spatial response function is shown in Figure 2-5, which highlights that modes of degree $l = 1$ are observationally favored for spatially-unresolved stars.

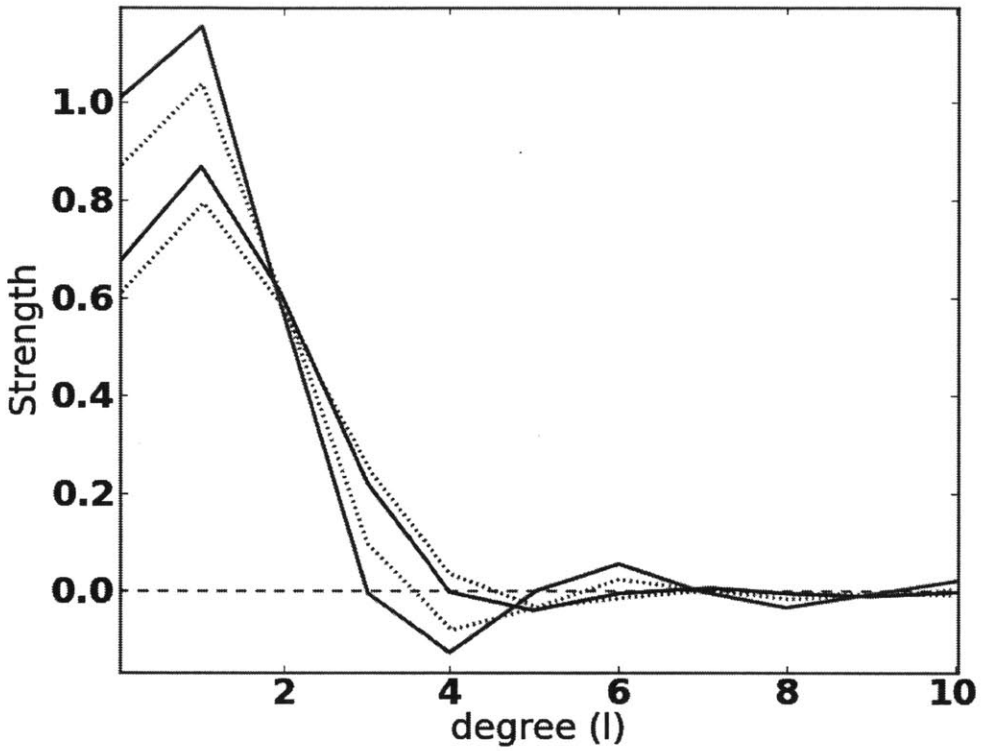

Figure 2-5: Spatial response functions integrated over a uniformly illuminated disk for different mode degrees, with m=0. (Note that a change in m corresponds to a change in the overall orientation of the harmonics. The effect of orientation is shown in Figure 2-6. The red model shows the response function in photometric data, while the blue model shows the expected response in RV measurements. The dotted lines account for limb-darkening of the form $W(\theta) = 1 - 0.75(1 - \cos(\theta)) + 0.22(1 - \cos^2(\theta))$ [54, 17]. A negative value of the spatial response function indicates that the overall response is less than the unperturbed reference.

There is an additional observational bias dependent on the star's inclination with the line of site. The relative power within any given mode for a star with inclination i is given by [26]:

$$\epsilon_{l,m}(i) = \frac{(l - |m|)!}{(l + |m|)!} \left[P_l^{|m|}(\cos(i)) \right]^2 \tag{2.16}$$

The relative mode power is shown in Figure 2-6 for various degrees and orders.

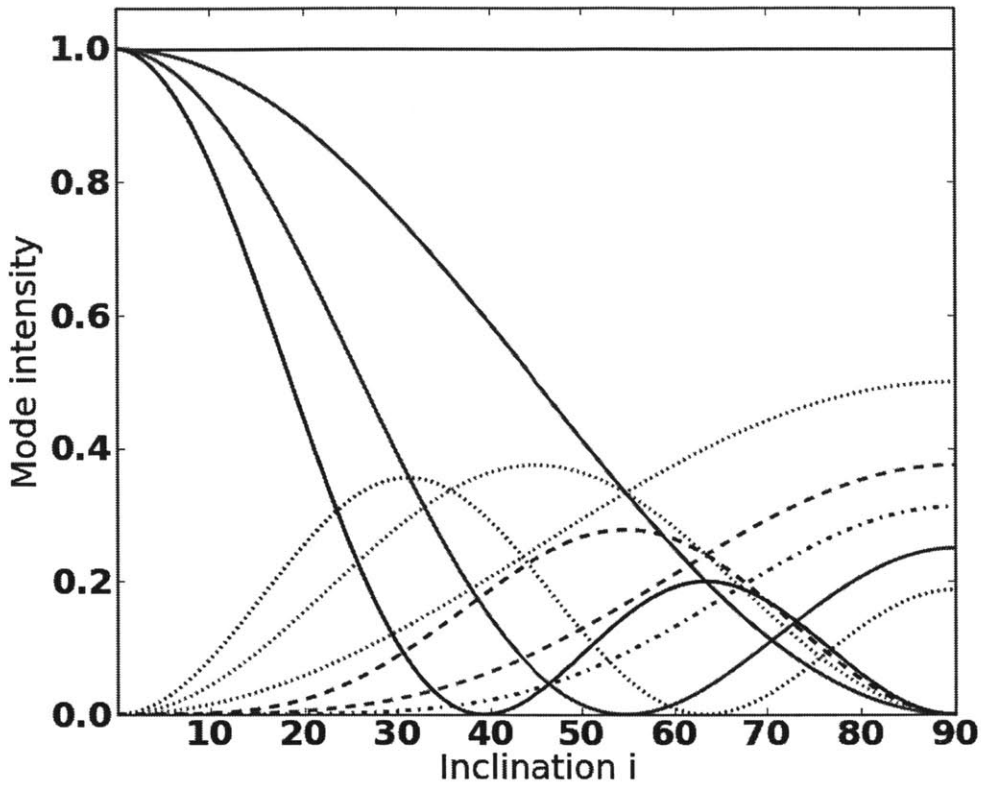

Figure 2-6: Mode visibility as a function of stellar inclination angle. Modes vary in l and m. Colors signify l values of 0 (blue), 1 (red), 2 (green) and 3 (black). Line styles represent m values of 0 (solid), 1 (dotted), 2 (dashed) and 3 (dot-dashed). [54]

For stars which can be spatially resolved (the Sun), the modes form a "comb" of frequencies with a Gaussian envelope centers on $\nu_{\max}$. The comb consists of alternating even and odd degree modes spaced by $\Delta\nu/2$ (following Equation 2.5), with odd modes typically of lower power than their even counterparts. The Suns RV spectrum is shown in Figure 2-7 for reference.

Echelle diagrams are typically used to study these modes. These plot the radial order or observed frequency against the frequency modulated by $\Delta\nu$. Deviation from the theoretical vertical lines indicates mixed modes or other second-order effects present. Compared to the sun, the RV spectra of other stars is typically sparse due

to shorter temporal baselines and the stochastic nature of the modes. An echelle diagram of the Sun is shown in Figure 2-8

2.5 Constraints on Radius from Interferometric Measurements

A direct measurement of the stellar radius using interferometry in conjunction with the asteroseismic measurements allows the stellar mass to be constrained with either a measurement of $\Delta\nu$ or $\nu_{\rm max}$, rather than both. This allows us to make two, independent estimates of mass. In general, astronomic interferometry synthesizes the signals received by several telescopes. Together these telescopes have a large effective diameter determined by their separation which allows the interferometer to create high-resolution images.

In the simplest case, a pair of radio telescopes have their voltage outputs multiplied and averaged, so that $\langle V_1 V_2 \rangle = (\frac{V^2}{2})\cos(\frac{\vec{b}\cdot\hat{s}}{c}) \equiv R$, where V_1 and V_2 are proportional to the electric field produced by an astronomical point source, $\vec{b}$ is the vector baseline connecting the two antennas, $\hat{s}$ is a unit vector along the direction in which both telescopes point and c is the speed of light. $\frac{V^2}{2}$ is proportional to the sources flux density, S. R is also known as the correlator. This is generalized to an n-array of telescopes by using pairs of telescopes as baselines.

For an extended source, the correlator can be broken into its cosine (R_c) and sine (R_s) components which are calculated by integrating over the source. We define the visibility as $V_\nu(\vec{b}\cdot\hat{s}/\lambda) = R_c - IR_s$. By definition the visibility is normalized such that $V_\nu(0) = 1$.

For stars, the visibility as a function of $\vec{b}\cdot\hat{s}/\lambda$ can be fit to the Fourier transform of a uniformly bright disk or the Airy function. This is a function of $\theta_{UD}(\vec{b}\cdot\hat{s}/\lambda) \equiv \theta_{UD}(b/\lambda)$, where θ_{UD} is the measured angular diameter of the object:

$$|V| = \left|\frac{2J_1(\frac{\pi\theta_{UD}b}{\lambda})}{\frac{\pi\theta_{UD}b}{\lambda}}\right| \tag{2.17}$$

where J_1 is the first order Bessel function.

However, stars experience limb-darkening, a phenomenon in which the edges of the star appear dimmer due to the lower optical depth. A first-order limb-darkened disk model is sufficient to correct for this effect [11]:

$$V = \left(\frac{1-\mu_\lambda}{2} + \frac{\mu_\lambda}{3}\right)^{-1}\left[(1-\mu_\lambda)\frac{J_1(x)}{x} + \mu_\lambda(\pi/2)^{1/2}\frac{J_{3/2}(x)}{x^{3/2}}\right] \tag{2.18}$$

where $x = \pi b\theta_{LD}/\lambda$, $J_n(x)$ is the n^{th} order Bessel function and θ_{LD} is the angular diameter corrected for limb-darkening. μ_λ is the limb-darkening coefficient dependent on stellar parameters.

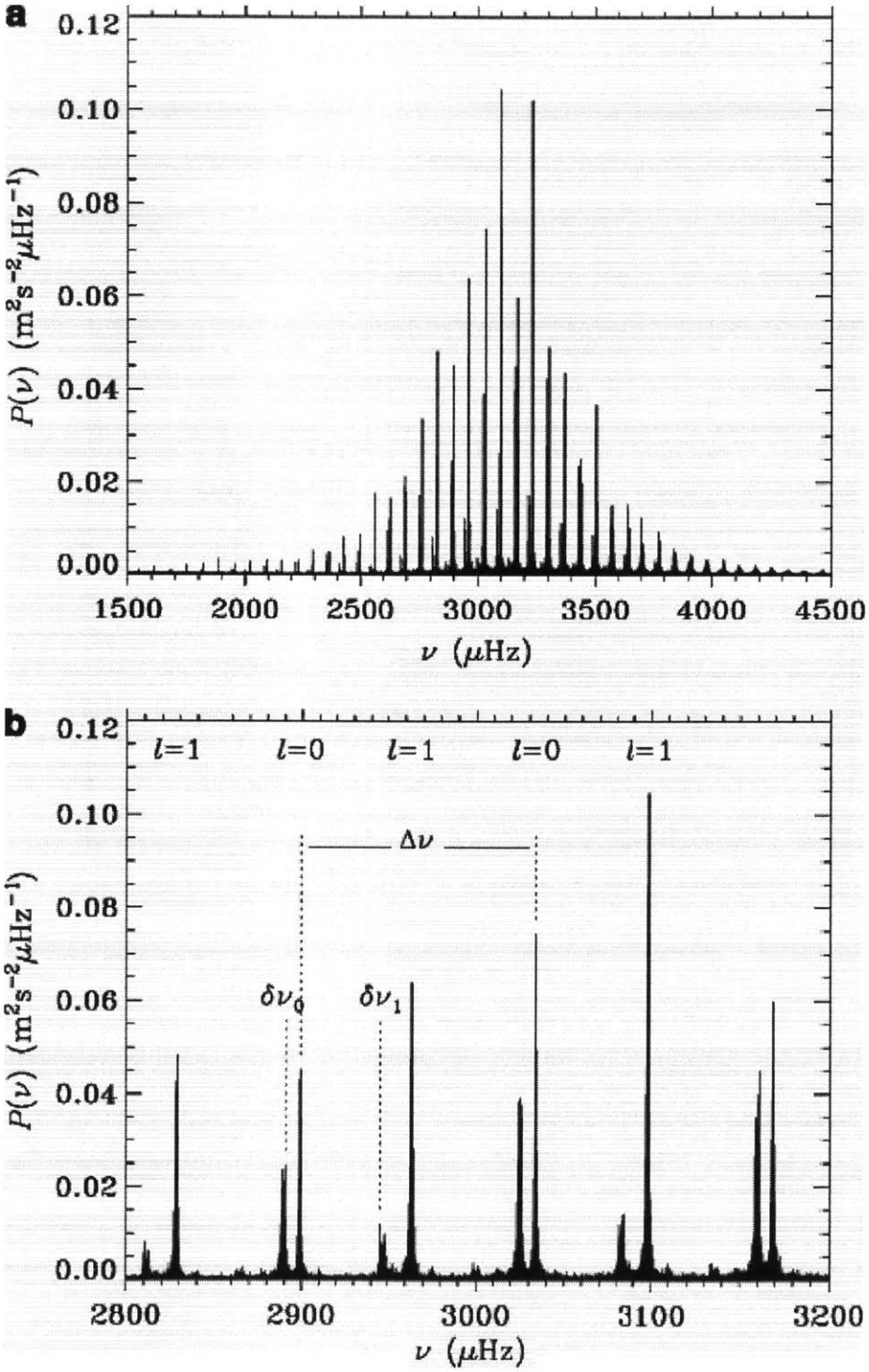

Figure 2-7: Power spectrum of solar oscillations, obtained from radial velocity measurements in light integrated over the full disk of the Sun. The data has a temporal baseline of approximately 15 years, revealing incredible details in the velocity spectrum. Panel (b) shows a zoomed-in version of panel (a) and highlights the standard asteroseismic observables, as well as the degree classification for a selection of the models. Figure taken from Aerts et al. (2010) [2].

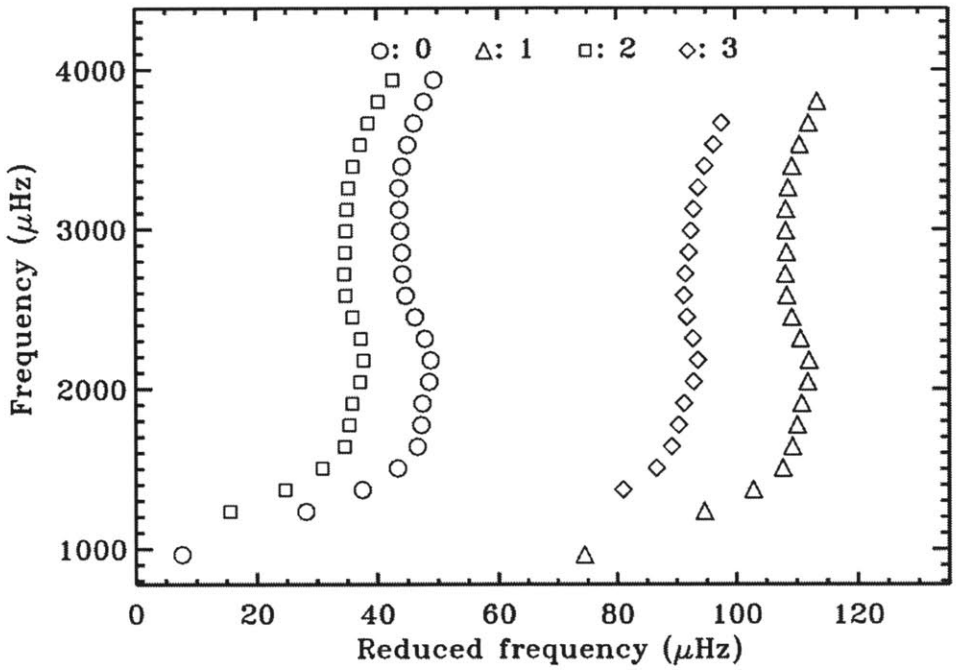

Figure 2-8: Echelle diagram for observed solar frequencies obtained with the BiSON network. The frequencies are modulo $\Delta\nu = 135\mu$Hz (described as "reduced" frequency) with $\nu_{\max} = 830\mu$Hz. The degree of the modes are indicated by the shapes. The deviation from the expected vertical-line model is evident for very low frequencies. Figure from Aerts et al. (1996) [2].

Chapter 3

CHIRON Radial Velocity Measurements

3.1 Target Selection

HD 82074 ($\alpha = 09^o\ 29'\ 32''.41$,$\delta = -04^o\ 14'\ 47''.88$, J2000) is a yellow G6 subgiant located in the constellation Hydra [59]. It has an apparent V magnitude of 6.26 and a distance of 56 ± 2 parsecs. We selected HD 82074 from a collection of nearby subgiants which have been previously observed and analyzed spectroscopically by our team. This will allow us to directly compare the results of the spectroscopic modeling and the asteroseismic results. Within this dataset, we select a subgiant which is visible from Cero Tololo within the spring observational period. We additionally choose a star which has an expected oscillatory signal ($\sim$ 2.2 m/s for HD 82074) which is larger than the instrumental limitations ($\sim$ 1.5 m/s). Additionally, the star must be relatively bright both to achieve a high signal to noise ratio (SNR) and to keep the duty cycle relatively short. HD 82074 has a predicted $\nu_{\max} \sim 200\mu$Hz from spectral analysis (see below), corresponding to an oscillatory period of $\sim$ 85 minutes. With an apparent V magnitude of $\sim$6.3, we expect the integration time around 13 minutes, or around 15% of the predicted period.

HD 82074 was previously analyzed using the Spectroscopy Made Easy (SME) software [56]. SME generates synthetic spectra by simulating radiative transfer through

the atmosphere of a star using Kurucz models and atomic line data available from the Vienna Atomic Line Database [46, 58]. SME is able to vary abundances, temperature, surface gravity, oscillator strengths, rotational velocity and micro/macro-turbulence within the star. Typically, the effective temperature, luminosity and metallicity are inputted parameters. The observed spectra are matched to the synthetic spectra and best parameters are found using a Levenberg-Marquardt minimization [53, 58]. The models produced by SME can be used to create a grid of evolutionary models, which are interpolated to estimate uncertainties in stellar properties (as discussed in Chapter 2) [30].

From this analysis, it is predicted to have a mass of 0.93 ± 0.6 $M_{\odot}$and a radius of $3.94 \pm 0.13 R_{\odot}$. With these parameters, we estimate a period of 83.3 minutes and amplitude of $\sim$2.16 m/s a frequency spacing of $\sim$ 16.65μHz using Equations 2.12a, 2.12b.

3.2 Observational Strategy

To devise an efficient observing strategy, we model the expected RV source and simulate our ability to accurately predict the stellar parameters. We generate a comb of frequencies spaced by $\Delta\nu/2$ with a broad Gaussian envelope, as shown in Figure 3-1. Because the excitation of modes is a stochastic process, we allow each frequency mode to be produced by a discrete string of excitations which have an e-folding time of $\sim$3 days. (An example of the process is shown in Figure 3-2). The true mode lifetime of subgiants is highly uncertain, ranging from 3-7 days [14]; we choose the lower bound of this range as a precaution. The amplitude and lifetime of each mode is selected randomly from Gaussian distributions centered on their expected values.

We compare the results of our model with RV data taken of HD 142091 with the HIRES spectrometer on Keck, using the same cadence and temporal baseline. HD 142091 is a known subgiant host star of an exoplanet with an orbital period of 1251$\pm$ 15 days and $m_p \sin i$=1.6 Jupiter masses [51, 35]. With the orbital solution removed, the subgiant exhibits oscillations characteristic of asteroseismology, with an amplitude of a few meters per second and a period of $\sim$1 hour. Although the baseline

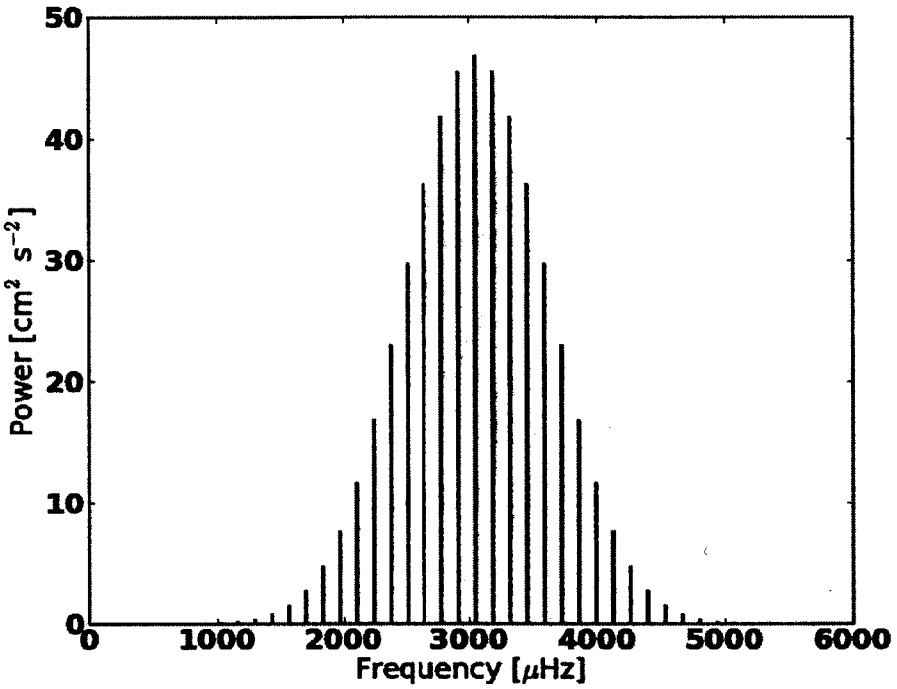

Figure 3-1: Sample of the Gaussian envelop of frequencies used to generate the simulated stellar oscillations. Solar parameters were used to generate this figure.

for this observation is too short to measure any asteroseismic parameters, we are able to successfully recreate datasets with similar amplitudes and frequencies using our model. Figure 3-3 shows a sample data set compared to the HIRES data.

We adjust the cadence for the expected integration time ($\sim$ 12 min for a SNR of 100) and the expected error from the CHIRON instrument ($\sim$ 1.5 m/s) in the form of Gaussian noise. We vary total days observed, hours observed per night and the temporal gap size between nights of observation.

We find that $\sim$ 8 days is sufficient to recover $\Delta\nu$ for a subgiant to within 10%, given a minimum of $\sim$ 4 hours of observation per night. The results for a simulation of HD 142091 is shown in Figure 3-4. We follow these general guidelines when requesting observational time.

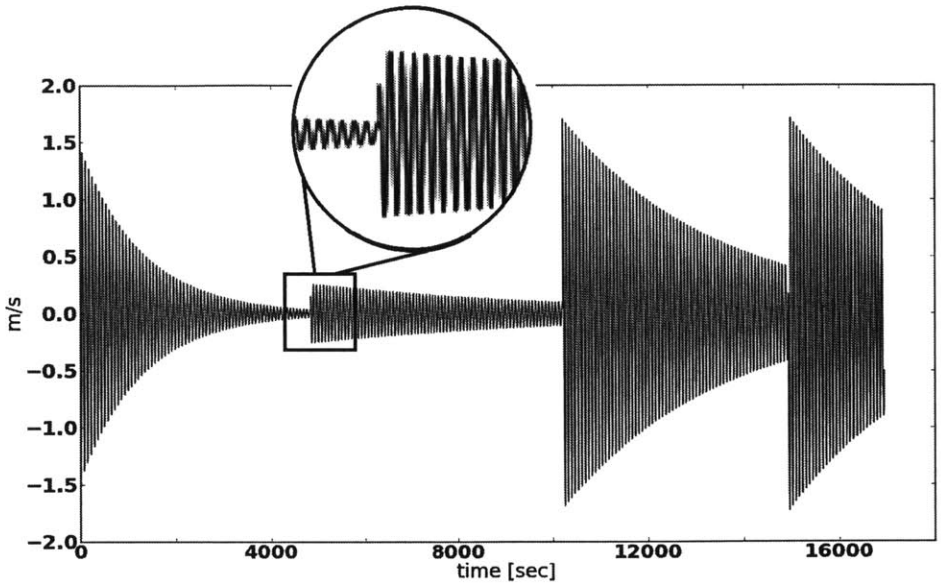

Figure 3-2: Sample of a mode excitation for an average mode lifetime of 1 day and average amplitude of 1 m/s. Note that each simulation uses tens of modes to fully simulate the asteroseismic signal, but only one such mode is shown in this Figure. Each excitation has a decay time and lifetime (time until which the next mode is excited) chosen from a Gaussian distribution centered on 1 days and 3 days (or 3 e-folding times). The amplitude of each excitation is chosen from a Gaussian distribution which is centered on the expected value from the comb of frequencies, such as those shown in Figure 3-1. Each distribution has a width of half its central value. The period of the oscillation is one hour. The inset, circular window is a zoom-in of the outlined region.

3.3 CHIRON Observations

We observed HD 82074 on the 1.5m telescope at CTIO in Chile. CHIRON is a highly stable cross-dispersed, fiber-fed echelle spectrometer which has demonstrated 1 m/s precision in RV spectroscopy. This accuracy is obtained using an iodine-cell calibration method [12, 34]. In this technique, starlight is sent directly through an iodine absorption cell in the spectrometer entrance slit. The cell provides hundreds of lines which can be used as calibrations for RV measurements, and each line encodes the intrinsic spectrometer point spread function (PSF). The PSF model is created by observing a nearby, rapidly rotating B star. These stars are essentially featureless blackbodies which imprint no additional lines on the iodine template. To recover RV

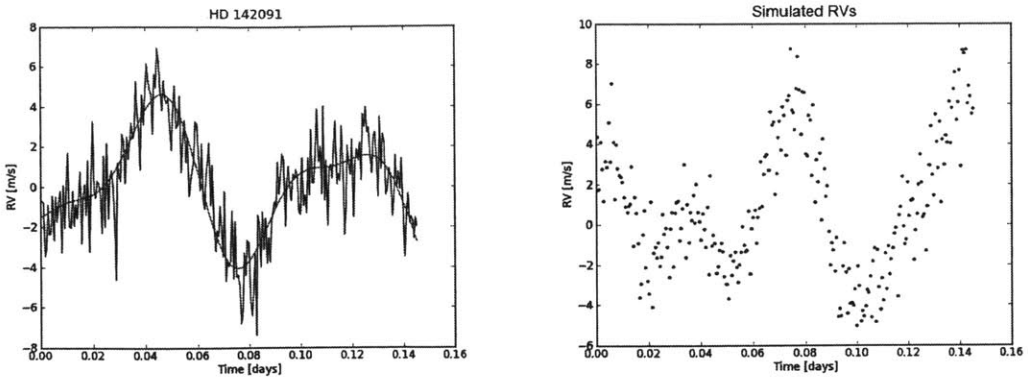

Figure 3-3: Comparison of real RV data and simulated data. The left panel is data taken from the Keck telescope of HD 142091 (blue) with a fit of multiple sine waves (green). The right panel shows simulated RV data using the same temporal baseline and sampling for a star with similar properties to HD 142091. Twelve modes are activated in this model, which were generated using $M_* = 1.8M_\odot$, $R_* = 4.71R_\odot$ and $L_* = 12.3L_\odot$, the parameters found using SME fitting in Johnson et al. (2008).

measurements, method works as follows: A deconvolved stellar template is taken of the target with a higher SNR and resolution than other observations but without the iodine cell in place. The theoretical iodine template is then multiplied by this stellar template and the product is convolved with the PSF. This spectrum is then used as a template for other observations. The radial velocities are extracted by comparing observed spectra to synthetic spectral models which allow for the wavelength scale, spectrometer PSF and Doppler shift to act as free parameters . For HD82074, we use HR 4172 as our calibration B star.

We observed in the wide slit mode (R=80,000-90,000 in the optical) from Feb. 12, 2014 to Feb 28, 2014 for a total of 8 nights. We measured for $\sim$ 3.5 hours each night. The calibrated data is shown below.

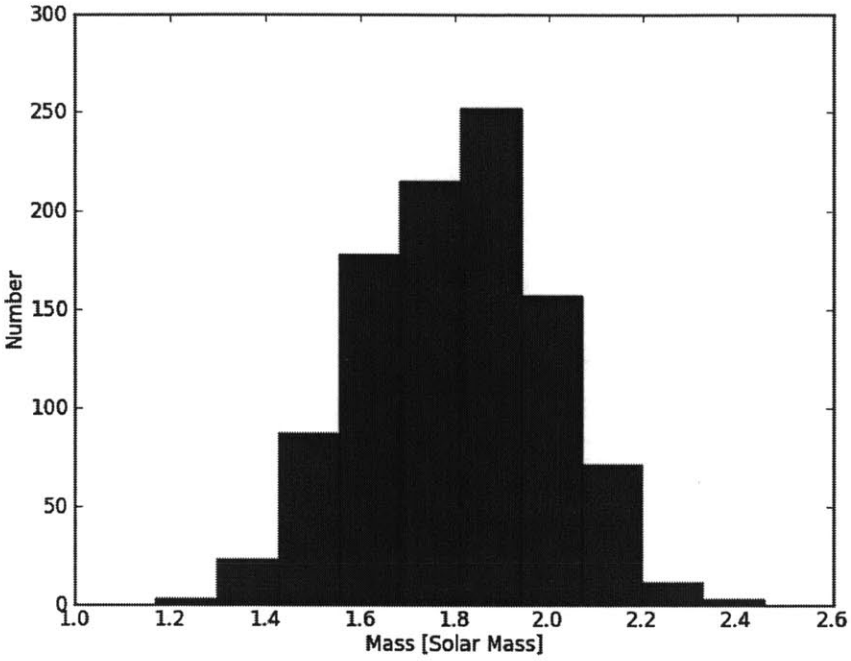

Figure 3-4: Histogram of 1000 simulated RV light curves on an 8 day baseline with 4 hours of observation per night. The input star has a properties matching HD 142091 with added Gaussian noise on the order of 15%. The derived mass distribution has a mean of $1.8M_{\odot}$with standard deviation of $0.19M_{\odot}$.

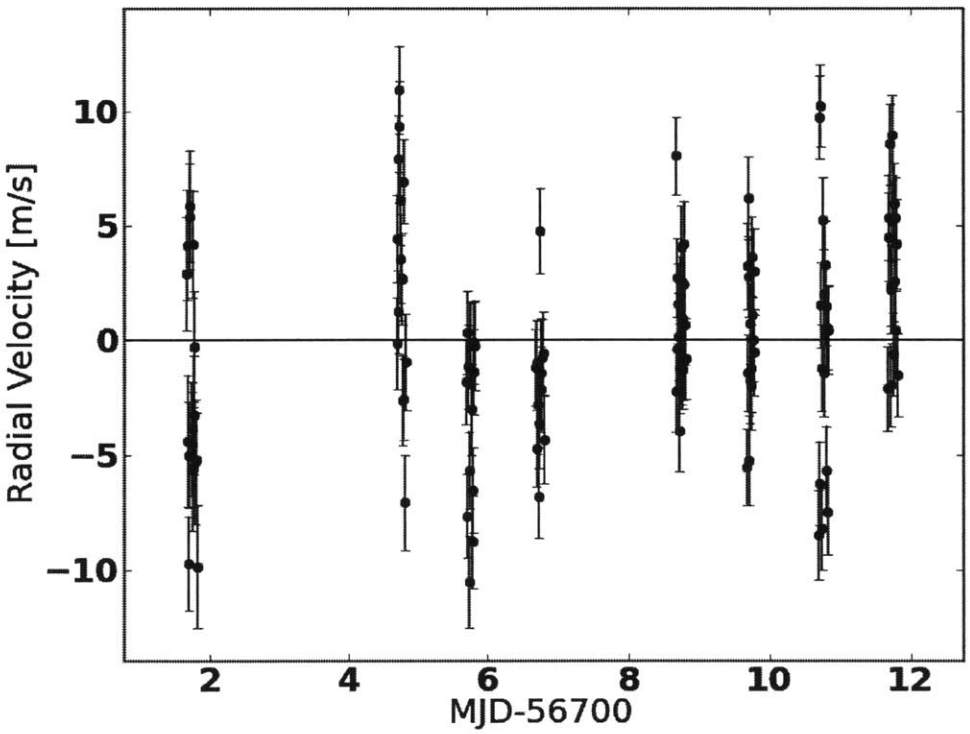

Figure 3-5: RV data and associated errors over all 8 nights.

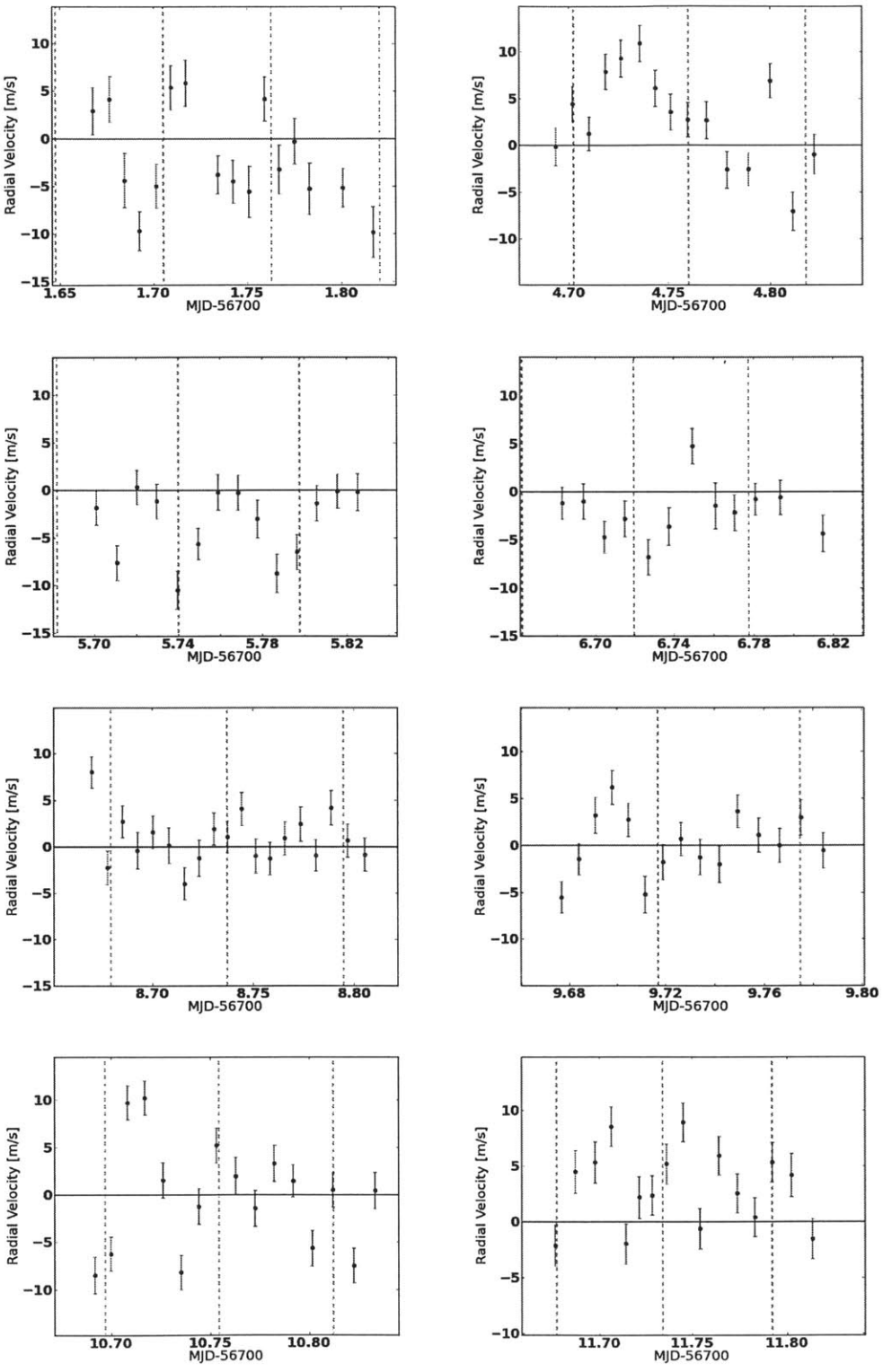

Figure 3-6: RV data for each night shown in blue, with associated errors. Grey dashed lines are spaced by 83 minutes, the expected maximum-amplitude period for stellar mass and radius estimated using SME.

Chapter 4

CHARA Interferometric Observations and Results

4.1 CLASSIC Observations

We use the CHARA array on Mt. Wilson, California to directly measure the radius of HD 82074 given the parallax of 17.97 ± 0.50 microarcseconds [59]. This measurement will allow us to tightly constrain the asteroseismic data, and thus the mass of the star. The CHARA array is an interferometric array of six telescopes, each with a 1-meter diameter. The array is capable of $\sim$200 microarcsecond resolution.

We use CHARA in the CLASSIC observational mode which uses two telescopes within the array. We observed in the H-band which has an effective wavelength of 1.673 microns. The data were taken between March 3, 2014 and April 21, 2014. The data is shown in Table 4.1. Calibrators with known angular diameters were selected from the JMMC Stellar Catalogue and used to estimate visibility errors [39].

We model HD 82074 using the limb-darkened disk model (Equation 2.18). We use the effective wavelength of CHARA's H-band filter for λ. The linear limb-darkening coefficient (μ_λ) is determined by interpolating the ATLAS model grid by Claret & Bloeman (2011) to the spectroscopic estimates of $T_{\rm eff} = 4996 \pm 44K$, $\log g = 3.22 \pm 0.06$ dex and [Fe/H] $= -0.43 \pm 0.3$ dex. We note that our surface gravity, $\log g$, is one of the uncertain parameters derived from SME. We therefore calculate limb-darkening

Table 4.1. Summary of CHARA Observations

MJD	Baseline [m]	Visibility	Error	Calibrators
56730.182	305.09	0.6336	0.0569	HD 82043, HD 86694
56730.197	310.6	0.6423	0.0211	HD 82043, HD 86694
56730.211	313.04	0.6296	0.0556	HD 82043, HD 86694
56737.186	312.16	0.6661	0.0384	HD 82043, HD 86694
56737.196	313.41	0.6549	0.0379	HD 82043, HD 86694
56768.234	249.08	0.7279	0.0264	HD 82043, HD 86694
56768.265	247.93	0.759	0.0508	HD 82043, HD 86694

coefficients for $\log g$ ranging from 2.5 to 4 dex. This corresponds to a $\sim 80\%$ error in the calculated surface gravity, which could arise from an 80% error in mass or 50% error in radius. Within this range (and the range of [Fe/H]'s uncertainty), the value of μ_λ ranges from 0.3364 to 0.3406 in the ATLAS model. This change in μ_λ has no discernable effect on the model. We adopt $\mu_\lambda = 0.3385$, the average, for our analysis.

We use a Levenberg-Marquardt minimization algorithm to minimize the χ^2 value of our fits to both a uniform disk model and a limb-darkened model for our seven data points. Each model has one degree of freedom. We find that $\theta_{UD} = 0.641 \pm 0.007$ mas and $\theta_{LD} = 0.662 \pm 0.007$ mas. The uniform-disk model and limb-darkened model fits have χ^2 values of 2.20 and 2.17, respectively. They are shown in Figure 4-1. Using this angular diameter and a parallax of 17.97 ± 0.50 mas, we calculate a solar radius of $3.96 \pm 0.12 R_\odot$.

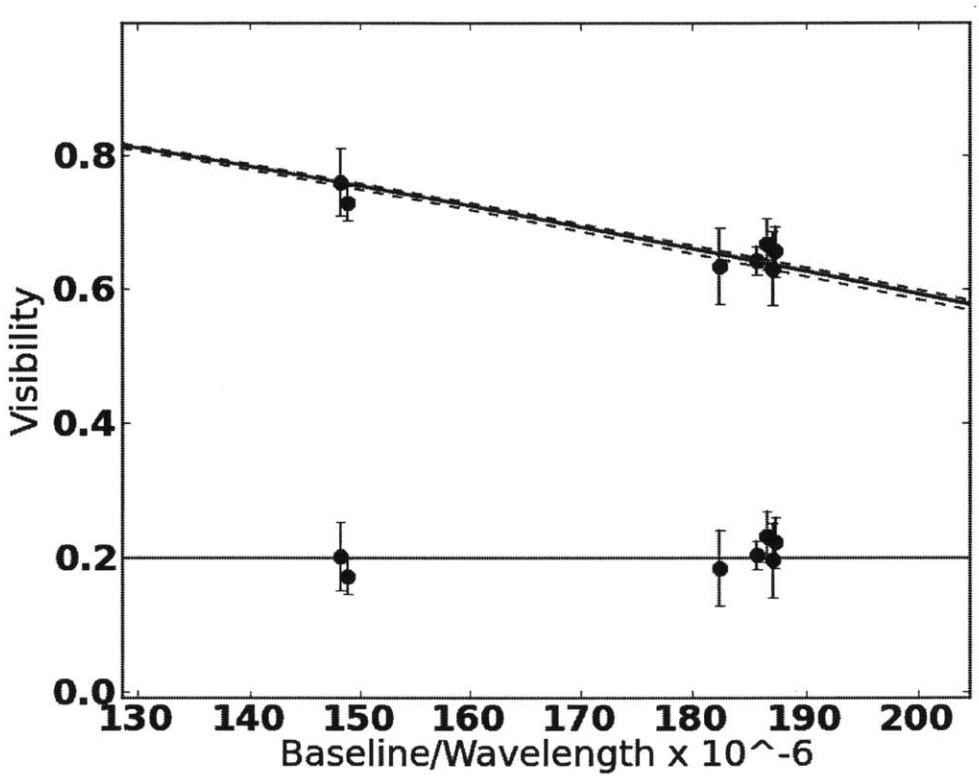

Figure 4-1: CHARA interferometric measurements and best fit models. The blue solid line indicates the best-fit, limb-darkened model. The blue dashed lines show the 1-σ uncertainties. The best-fit uniform-disk model is also overlayed in green, but is not distinguishable from the limb-darkened models.

Chapter 5

Analysis

5.1 Significance Spectra

To analyze the RV time series we make use of the SigSpec algorithm [48]. SigSpec, short for "Significance Spectrum", is a statistical technique used to analyze noisy and unevenly sampled data. SigSpec is an extension of Lomb-Scargle least-squares spectral analysis method (LSSA). LSSA (and Sigspec) modifies the discrete Fourier transform by introducing artificial time gaps to shift observations to equally-sampled times. SigSpec additionally calculates the likelihood that the amplitude of the observed signal could be obtained if the data were noise. This likelihood is given as the measurement *sig*:

$$sig(A) = \frac{RA^2 \log(e)}{4\langle v^2 \rangle} \cdot sock \tag{5.1}$$

where A is the calculated amplitude of the angular frequency (ω), R is the number of pairs (t_r, v_r) in the time series, $\langle v^2 \rangle$ is the variance of the RVs, and *sock* is defined as the function:

$$sock(\omega, \theta) = \left[\frac{\cos^2(\theta - \theta_0)}{\alpha_0^2} + \frac{\sin^2(\theta - \theta_0)}{\beta_0^2} \right] \tag{5.2}$$

Here, α_0, β_0 and θ_0 define the sampling profile:

$$\tan(2\theta_0) = \frac{R\sum_{r=0}^{R-1}\sin(2\omega t_r) - 2(\sum_{r=0}^{R-1}\cos(\omega t_r))}{(\sum_{r=0}^{R-1}\sin(\omega t_r))} \tag{5.3}$$

$$\alpha_0^2 = \frac{2}{R^2}\left(R\sum_{r=0}^{R-1}\cos^2(\omega t_r - \theta_0) - \left(\sum_{r=0}^{R-1}\cos(\omega t_r - \theta_0)\right)^2\right) \tag{5.4}$$

$$\beta_0^2 = \frac{2}{R^2}\left(R\sum_{r=0}^{r-1}\sin^2(\omega t_r - \theta_0) - \left(\sum_{r=0}^{R-1}\sin(\omega t_r - \theta_0)\right)^2\right) \tag{5.5}$$

The *sock* function is analogous to the spectral window used in DFT analysis. The spectral window is used to determine the effects of the time series sampling on the spectrum by taking the DFT of a constant series with the same time domain. Terrestrial data often suffers for daily gaps, which are seen in the spectral window as peaks at integer multiples of $\sim 1\mathrm{d}^{-1}$. Similarly, the *sock* function acts as weights for *sig* measurement in order to take into account the influence of the temporal sampling on the significance spectrum.

SigSpec iteratively removes the highest peak in the spectrum and checks its statistical significance. A cutoff *sig* limit of 3 (corresponding to a quoted $\frac{1}{1000}$ chance in finding that frequency from white noise) is chosen when generating the reduced significance spectra. A weighting of $1/\sigma_i^2$ is used for the associated measurements. The discrete Fourier transform of the 8 nights of data and the significance spectrum are plotted in figure 5-1.

We compare our power spectrum to noise by randomly rearranging the RV measurements and errors of the RV observations made with CHIRON while preserving the time sampling. For 1260 trials, we find that the median, maximum *sig* detected is 2.85. The distribution is skewed towards larger *sig* values. We find that nearly every simulation has a maximum *sig* detection of at least 2, while 44% have a maximum *sig* detection of 3, our cutoff *sig* value. The distribution is shown in Figure 5-2. The minimum *sig* value from our dataset that we consider in our analysis is 3.05, which lies in the 60^{th} percentile of the distribution. If we assume that our calculated distri-

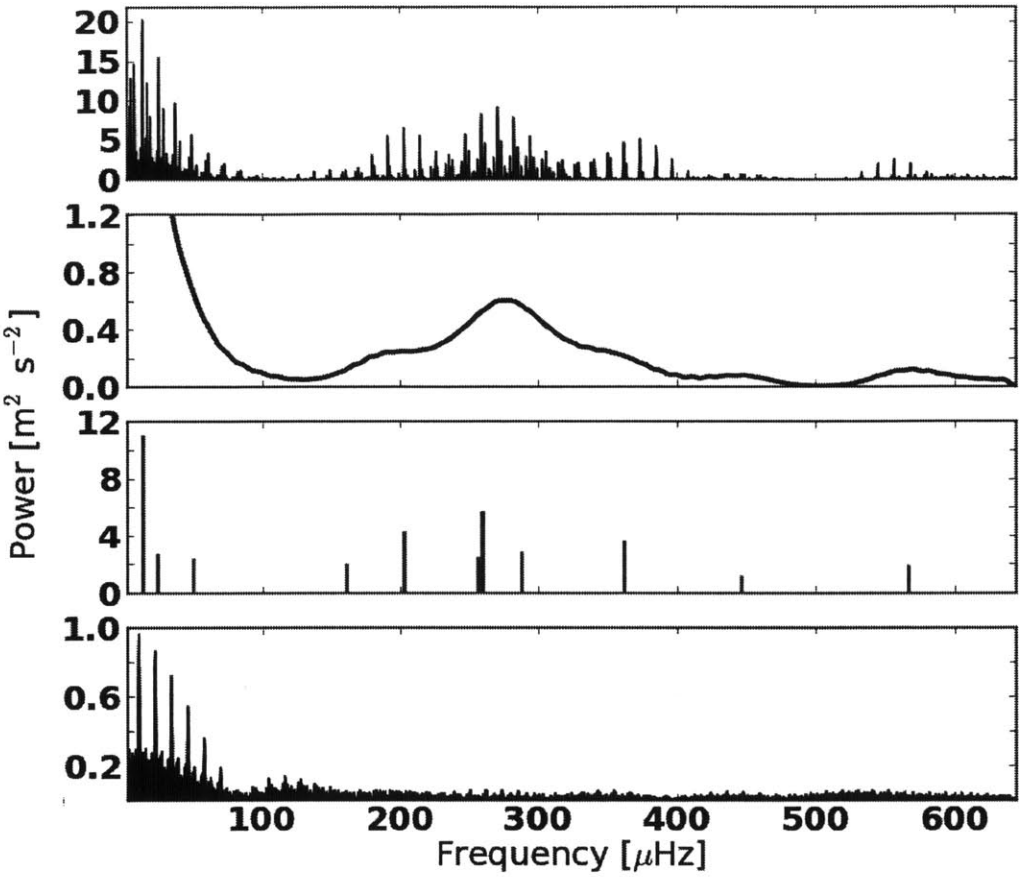

Figure 5-1: DFT Power spectrum of radial velocity measurements (top panel, second panel), its corresponding SigSpec spectrum (third panel) and the observational window function (bottom panel). In the SigSpec spectrum, blue lines indicate frequencies with $sig \geq 3$.. The red lines correspond to frequencies with $sig \geq 2$. The second panel shows the DFT power spectrum smoothing using a Hanning window of length 23μHz. The lower frequencies may be attributed to correlated noise or low-frequency stellar noise. There is a clear excess of power between 200μHz and 375μHz.

bution of trials is the true probability distribution of *sig*s from SigSpec, we find that each of our measurements have at most a 40% chance of arising from white noise. We explicitly state the measured frequencies, *sig* values and calculated probabilities of that each frequency arises from white noise in Table 5.1. Additionally, noise typically produces far fewer peaks with $sig \geq 2.0$ than the power spectrum produced by our dataset ($\sim$ 3 or fewer versus $\sim$ 7). An example periodogram of noise is shown in Figure 5-3 for comparison. 203, 257, 260, 287 and 362

Table 5.1. Measured Significant Frequencies

Frequency [μHz]	*sig*	P(noise)
203	3.39	0.22
257	3.22	0.30
260	3.56	0.16
287	3.48	0.19
362	3.05	0.38

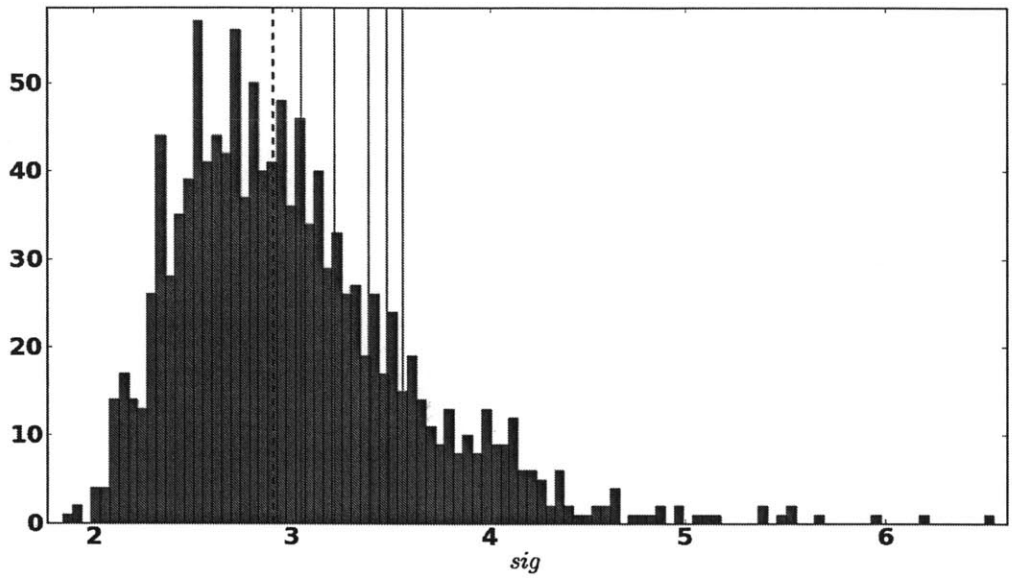

Figure 5-2: Distribution of *sig* values for 1260 simulations of noise. The blue, dotted line indicated the median value of 2.85. (The mean value of the distribution is 2.9). Red lines indicate calculated *sig* values from our dataset.

5.2 Determining $\nu_{\max}$

Because the modes are excited stochastically, it is very difficult to accurately measure $\nu_{\max}$ without a long temporal baseline. The amplitude of each mode varies around an average amplitude with each excitation. The baseline should be longer than several mode lifetimes in order to these averages of each mode. For shorter baselines, the theoretical Gaussian comb of frequencies in the RV power spectrum (described in Chapter II) is generally not seen, leading to large uncertainties in $\nu_{\max}$.

The significant detections in Figure 5-1 at low frequencies $\leq 50\mu$Hz either correspond to temporally correlated error in the CHIRON measurements or granulation of

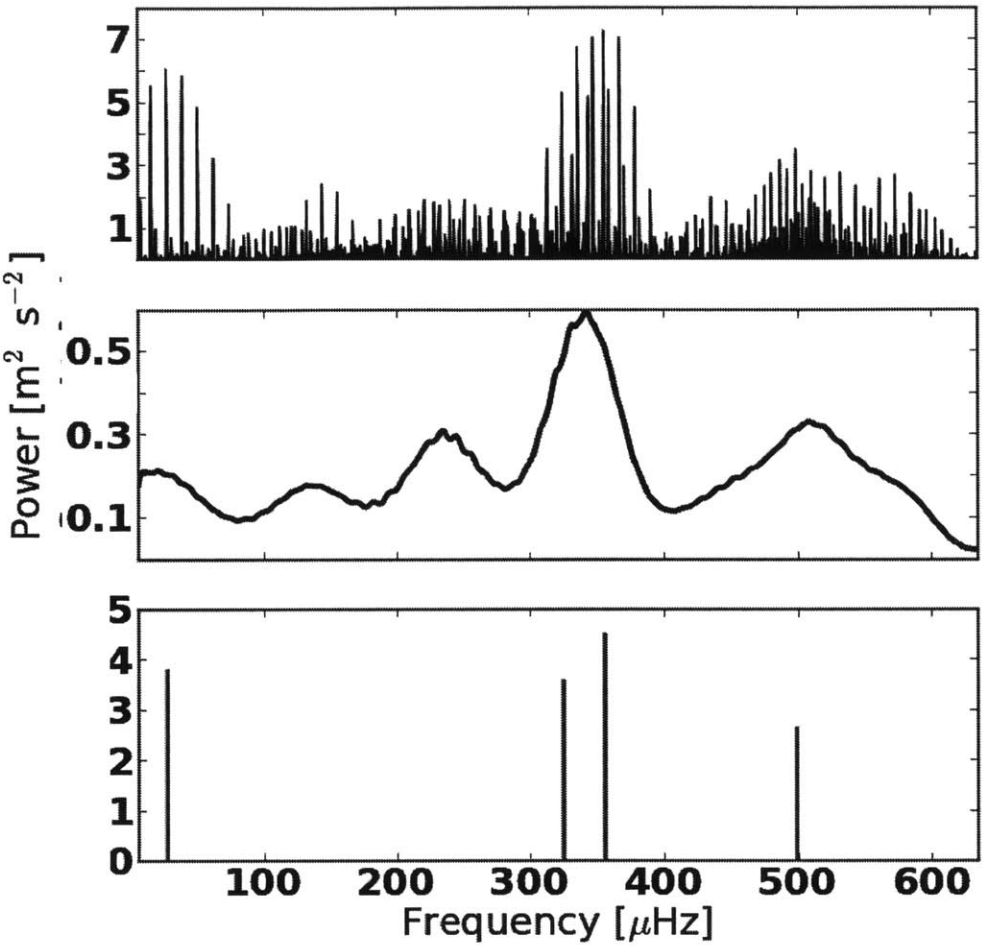

Figure 5-3: DFT Power spectrum of shuffled radial velocity measurements (top panel, second panel), its corresponding SigSpec spectrum (third panel) to simulate non-periodic noise. The same temporal cadence and baseline is used. The red lines correspond to frequencies with $sig \geq 2$. There were no frequencies detected with $sig \geq 3$. The second panel shows the DFT power spectrum smoothing using a Hanning window of length 23μHz.

the star and is therefore unlikely to be due to an asteroseismic signal [48]. Assuming the radius measured by CHARA, the detected signal at $\sim 566\mu$Hz would correspond to a mass of $2.7M_{\odot}$, which is well above the mass predicted through spectroscopy ($M_* = 0.93 \pm 0.06$). It is therefore most likely that the maximum frequency ($\nu_{\max}$) lies within the excess power seen between 150μHz and 400μHz. We detect five signifi-

cant peaks in the power spectrum between 150μHz and 400μHz, at 203, 257, 260, 287 and 362 μHz. The weighted average of these frequencies (taking the significance values to be weights), the average frequency is 239μHz. We take the range of significant frequencies found as the error on our maximum frequency. Using $\nu_{\rm max} = 239^{+123}_{-36}\mu$Hz and Equation 2.12a:

$$R = (7.84 \times 10^{-2})\frac{\nu_{\rm max} T_{\rm eff}^{1/2}}{\Delta\nu^2}{\rm R}_\odot \tag{5.6}$$

and the measured radius of HD 82074 using CHARA (3.96R$_\odot$), this corresponds to a mass estimate of $1.14^{+0.59}_{-0.19}$M$_\odot$.

5.3 Determining $\Delta\nu$

The autocorrelation of the discrete Fourier transform of the RV data (shown in Figure 5-4 shows no sign of excess power in the expected frequency range, apart from daily aliasing at multiples of 11.57μHz, indicated that there is no clear detection of $\Delta\nu$.

To measure $\Delta\nu$, we instead make use of the echelle diagram. Using equation 2.5, we match the observations with expected $\nu_{n,l}$ and fit parameters $\Delta\nu$ and ϵ. We take the small separation, $\delta\nu$, to be $0.08\Delta\nu$ based on Figure 5-5.

We use a Markov Chain Monte Carlo to fit the most significant frequencies ($sig \geq 3.0$) to the second-order model describes in Chapter II. This model simply consists of four vertical lines in the echelle diagram, representing degrees of 0 to 3. Because we have chosen $\delta\nu = 0.08\Delta\nu$, we reduced the degrees of the model to two: $\Delta\nu$ and ϵ. $\Delta\nu$ determines the distance between the vertical lines, while ϵ determines the horizontal overall shift. Therefore, we aim to maximize the likelihood:

$$\mathcal{L} = -0.5\sum_{i=1}^{n}\chi_i^2 - \sum_{i=1}^{n}\log\left(2\pi(\sigma_i^2 + s^2)\right) \tag{5.7}$$

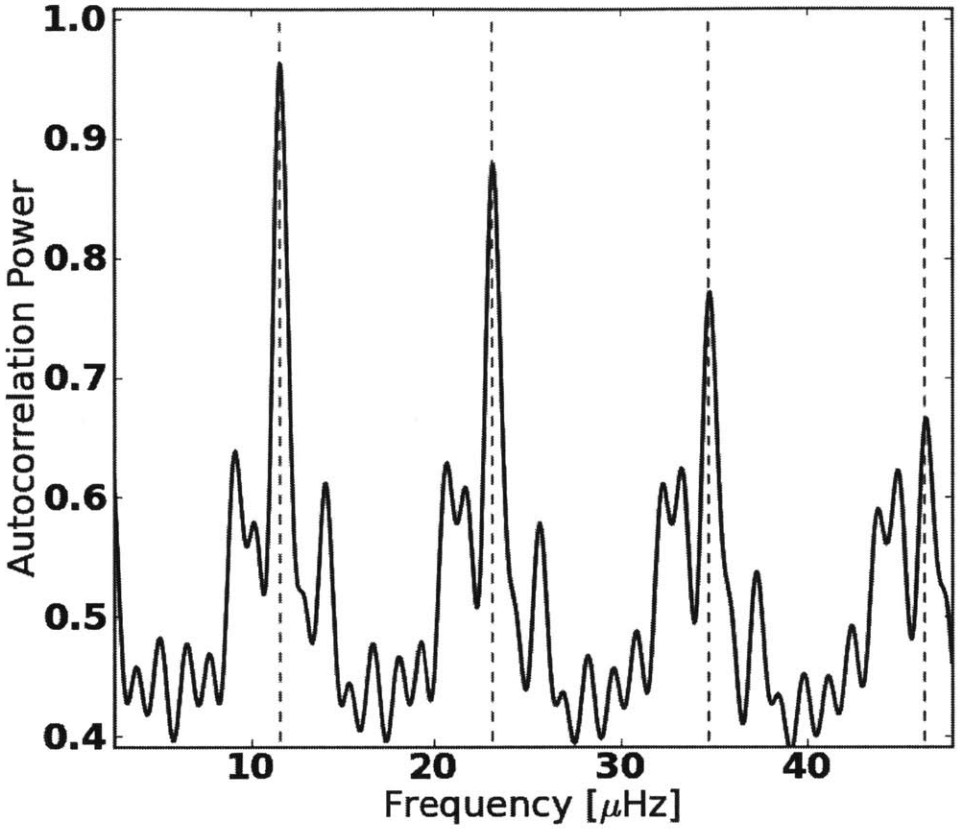

Figure 5-4: Normalized autocorrelation of the DFT. Dotted lines indicate the expected daily aliasing frequencies.

where,

$$\chi_i^2 = \frac{\min\left[(n + \frac{l}{2} + \frac{1}{4} + \epsilon - \nu_i)^2\right]}{\sigma_i^2 + s^2} \equiv \frac{(\nu_{\text{best}} - \nu_i)^2}{\sigma_i^2 + s^2} \tag{5.8}$$

Here ν_i is the i^{th} observed, significant frequency with associated error $\sigma_i \equiv \frac{1.14}{\sqrt{sig}}$ where 1.14 is the theoretical frequency resolution (in μHz) defined by the reciprocal of the total temporal baseline. s is an additional term to account for addition uncertainty in the frequencies not account by σ_i. We allow n to vary from 0 to 40 and l to vary from 0 to 3 in the calculation of the predicted frequency. We minimize the difference between the predicted and observed frequency in our calculation of χ^2.

We use the stellar radius measured from the interferometric data as a prior by

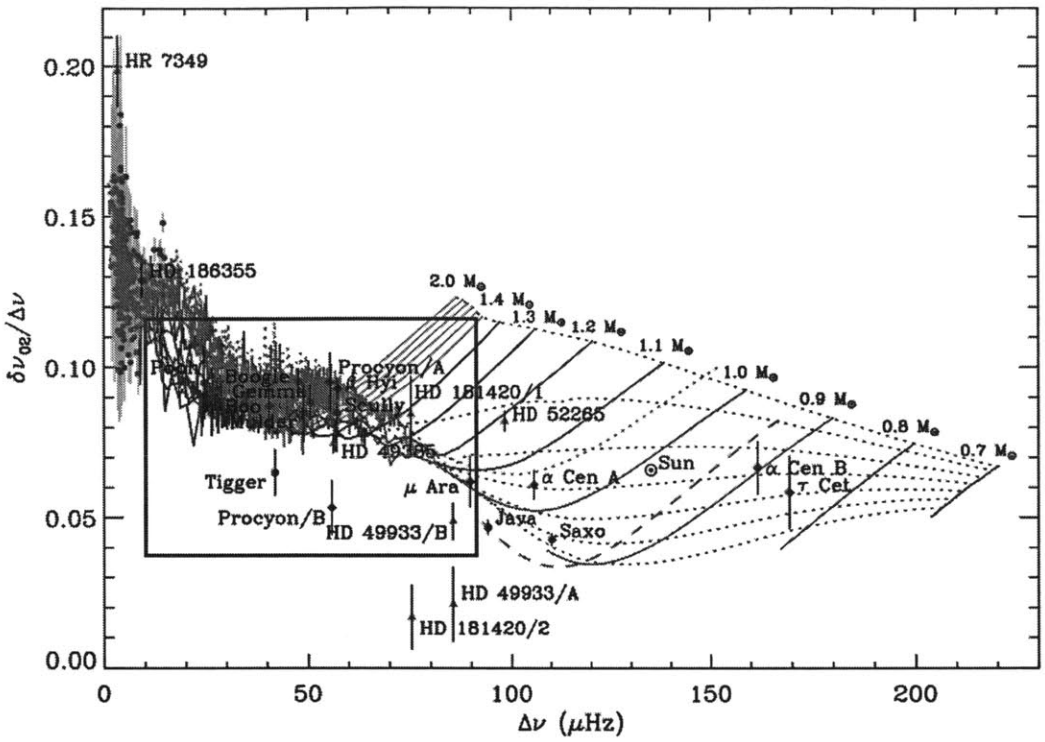

Figure 5-5: Diagram of $\Delta\nu$ vs the ratio of $\delta\nu$ to $\Delta\nu$. Solid lines show tracks for stars with metallicity Z_0=0.017, while dotted lines show tracks with metallicity Z_0=0.011 and dashed lines show tracks with metallicity Z_0= 0.028. Subgiants occupy the region outlined in the red box.

checking the self-consistency of the model. For each step of the MCMC, we test a new pair $(\Delta\nu_i, \epsilon_i)$. We use $\Delta\nu_i$, the measured radius and Equation 2.12a to calculate a theoretical mass. Using the theoretical mass predicted from $\Delta\nu$, the measured radius, the SME temperature and Equation 2.13 we can calculate a theoretical $\nu_{\rm max,th}$. Realistically, $\nu_{\rm max,th}$ should occur for an $0^{\rm th}$ degree mode ($l = 0$). Again using Equation 2.5 and our pair $(\Delta\nu_i, \epsilon_i)$, we choose the p mode defined by $\nu(n,0)_{best}$ which minimizes $|\nu_{max,th} - \nu(n,0)|$. We therefore establish the prior:

$$\exp\left(-\frac{(\nu_{max,th} - \nu(n,0)_{best})^2}{2\sigma_\nu^2}\right) \tag{5.9}$$

Where σ_ν is the uncertainty in $\nu_{max,th}$ propagated from the error of the radius measurement.

We run the MCMC for 500 iterations, with each iteration taking 500 steps through parameter space. We eliminate the first 50 steps of each trajectory to account for burn-in and average the final steps. Initial conditions are set broadly, with $0.7 \leq \epsilon \leq 2.0$ and $15.5 \leq \Delta\nu \leq 25.0$. The range of ϵ covers the entire physical range expected in most stars. The range for $\Delta\nu$ covers a mass range of $0.81 M_\odot$to $2.1 M_\odot$, given a radius of $3.96 R_\odot$.

We find that $\Delta\nu = 18.73^{+0.14}_{-0.04}\mu$Hz and $\epsilon = 1.10^{+0.48}_{-0.01}$. Note that these error bars do not include possible systematic errors. The scatter term, s is equal to $0.7^{+0.5}_{-0.6}$. Using Equation 2.10, this corresponds to a stellar density of $0.139 \pm 0.001 \rho_\odot$. The best fit has a $\chi^2 \simeq 2.49$, with two degrees of freedom (Δ_ν and ϵ) and 5 data points. This corresponds to a reduced $\chi^2 = 0.83$. The echelle diagram is shown in Figure 5-7, and the posterior distribution of the parameters is shown in Figure 5-8.

We check if this is a spurious result by generating five random "peak" frequencies between 200 μHz and 370 μHz (approximately the range in which we find peak frequencies) and fitting the noise to the same model. We assign each peak with a $sig = 3$, the cutoff power in our study. Because the uncertainty of each frequency goes as $1/sig$, this low sig value gives each peak maximal uncertainty. We run 280 iterations of the 500-walker MCMC on the noise. The distribution of χ^2 values for the best-fit solutions is shown in Figure 5-6. We find that the average, reduced χ^2 for the best-fit solution (the maximum in the posterior distribution) is $\simeq 17$, compared to our reduced χ^2 value of 0.83 from the data. We additionally find that 18 of the 280 (6.4%) have a $\chi^2 \leq 2$. Additionally, we find no iterations in which the best solution has $\chi^2 \leq 2$. and converges to a unique solutions ($\geq$50 MCMC walkers land within 1μHz of one another). Based on these results, we set an upper probability limit of 0.064 of finding a solution with reduced $\chi^2 \leq 2$ if our result were due solely to noise.

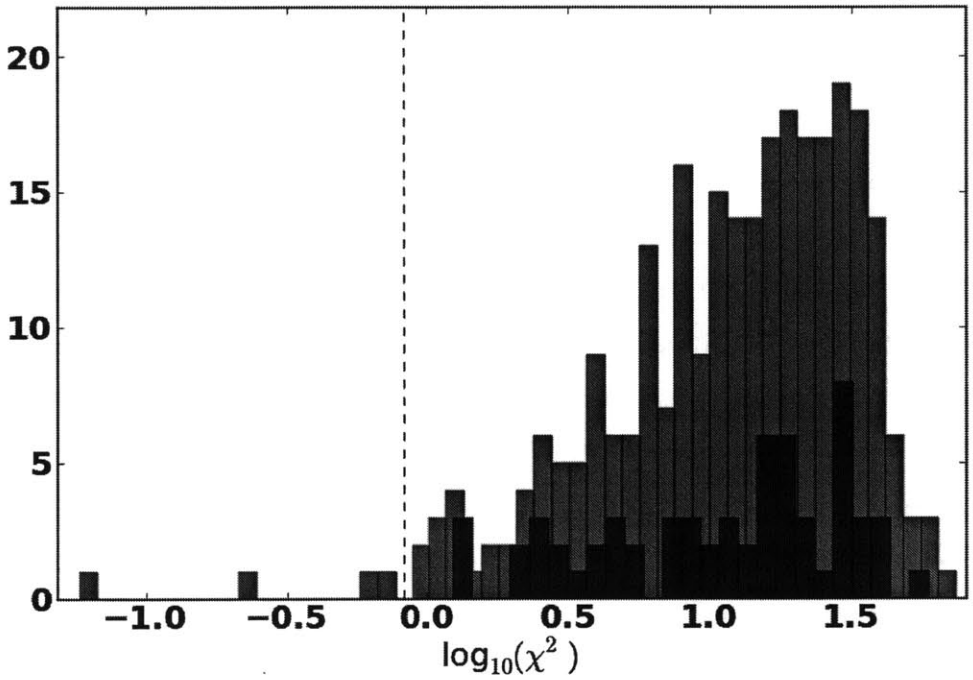

Figure 5-6: Distribution of reduced χ^2 values for the best-fit solutions to the echelle-diagram model derived from 500 MCMC iterations using noise. The blue bars represent the distribution of χ^2 values for the iterations which have a unique solution ($\geq$50 MCMC walkers land within 1μHz of one another). The red line indicates the reduced χ^2 of our fit to the dataset.

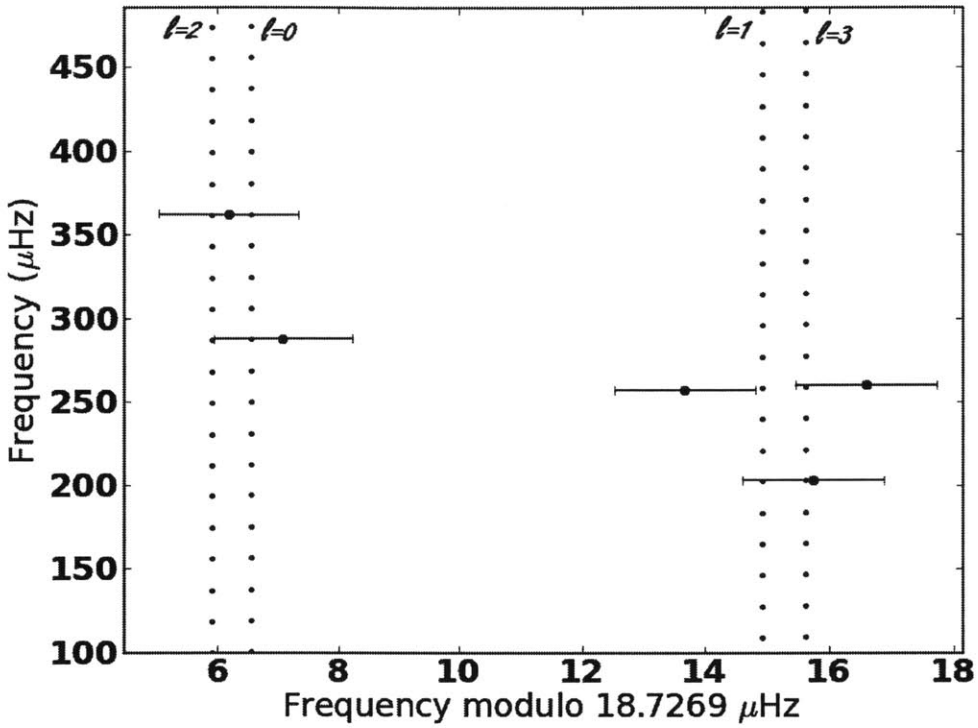

Figure 5-7: Echelle diagram for HD 82074 using $\Delta\nu \simeq 18.73$. Observed frequencies are shown in blue and the expected model is shown in red. Degree modes are indicated near the top of the panel. Error bars represent the theoretical resolution given the observational baseline divided by the squareroot of the significance.The reduced χ^2 of the fit is $\sim$0.83

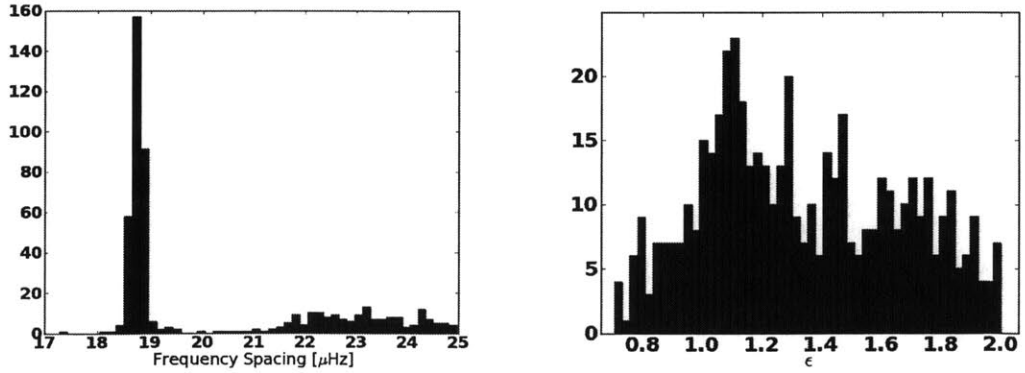

Figure 5-8: Posterior distributions for $\Delta\nu$ and ϵ for 500 simulations. In the posterior distribution for $\Delta\nu$, the solution between 18 and 19μHz contains $\sim$ 65% of the walkers, while the remainder is scattering between 21.5 and 25μHz.

Chapter 6

Results

We have observed solar-like oscillations in the subgiant HD 82074 and measured its radius interferometrically. We find that the radius ($3.96\pm0.12 R_\odot$) is in excellent agreement with the radius predicted using SME ($3.95\pm0.13 R_\odot$). Using $\Delta\nu$, ν_{max} and the radius, we apply Equations 2.12a and 2.12b to obtain mass estimates of 1.20 ± 0.11 $M_\odot$and $1.14^{+0.59}_{-0.19}$ $M_\odot$, respectively. The weighted average of these solutions is $1.19 M_\odot$; however, due to the large uncertainty on the ν_{max} estimate, we take the mass to be $1.20 \pm 0.11 M_\odot$. This estimate is more massive than the value suggested by spectral analysis ($0.93\pm.06 M_\odot$) by 2.45-σ. We summarize these results in Table 6.1.

We note that systematic uncertainties within our analysis have not been fully studied. Improvements can be made on eliminating excess background noise which may result in low-frequency granulation-changes of the star or instrumental errors. Such noise may bias significant detections to lower frequencies. Low-number statistics

Table 6.1. HD 82074 Parameters

	SME Value	Asteroseismic Value
Mass ($M_\odot$)	0.93 ± 0.06	1.20 ± 0.11
Radius ($R_\odot$)	3.95 ± 0.13	3.96 ± 0.12
$\Delta\nu(\mu Hz)$		$18.74^{+0.14}_{-0.04}$
$\nu_{max}(\mu Hz)$		239 ± 40
ϵ		$1.1^{+0.48}_{-0.01}$
T_{eff}(K)	4996 ± 44	
L ($L_\odot$)	8.64 ± 0.62	

and spurious detections may also plague our dataset. We found that our lowest-significant detection lies in the 60% percentile of a noisy *sig* distribution, implying that it may have risen from noise. However, the agreement of the independent mass estimates determined from $\Delta\nu$ and $\nu_{\max}$ seems unlikely to occur if our significant frequency detections are simply noise.

Additionally, the simplistic vertical-line echelle diagram model, while appropriate for the small number of data points, may be too simplistic to fully describe the frequency separation. In particular, subgiants are know to experience "avoided crossings" in $l = 1$ modes. This causes significant scatter around the $l = 1$ and $l = 3$ node lines in the echelle diagram. We would also greatly benefit from more RV data for both better resolution and the possibility of more significant frequencies. We have one additional night of CHIRON time scheduled, and additional PAVO CHARA data to be incorporated into this study.

The discrepancy we find in the mass estimates of HD 82074 made using SME and asteroseismology suggests that stellar models may underestimate their uncertainty or underestimate the mass of low-metallicity, low-density stars. A larger population of subgiants with properties similar to HD 82074 is necessary to further test the limitations of spectroscopy-based models.

HD 82074 adds to the growing population of asteroseismically studied subgiants with one of the lowest metallicities and densities. Its placement on an "HR diagram" of asteroseismology is shown in Figure 6-1. It serves as an important pivot point in grounding stellar models in the evolved branches of the HR diagram.

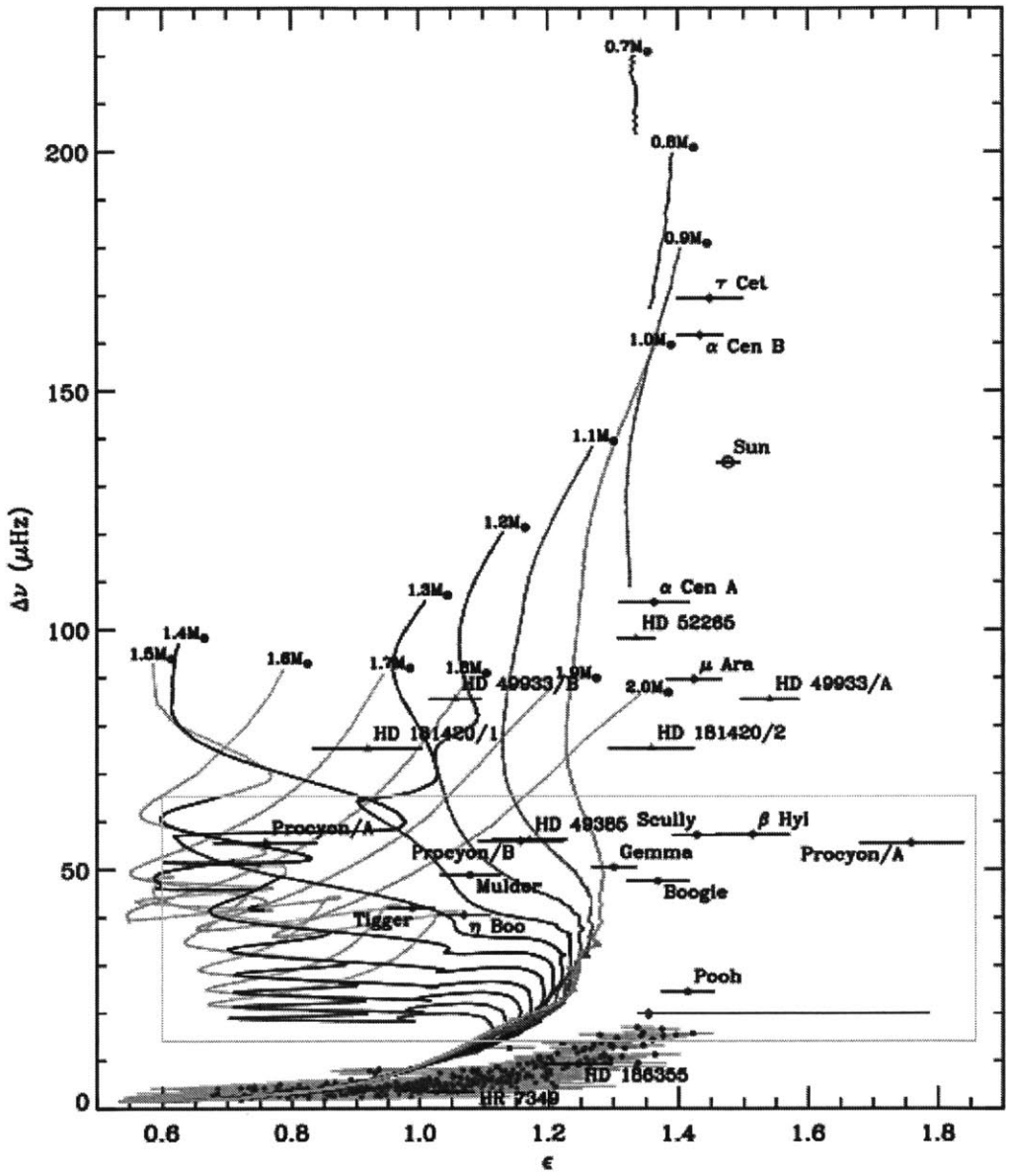

Figure 6-1: "Asteroseismology HR Diagram" from White et al. (2011) showing $\Delta\nu$ against ϵ. HD 82074 is shown with a large green diamond. The region of the diagram containing other subgiant stars is highlighted in yellow. Note that the subgiants have evolved off the main sequence, beyond the plotted tracks in this diagram [61].

Bibliography

[1] Conny Aerts and Christensen-Dalsgaard. *Asteroseismology.* Springer, 2010.

[2] Conny Aerts, Jørgen Christensen-Dalsgaard, and Donald W Kurtz. *Asteroseismology.* Springer, 2010.

[3] Judson L. Ahern. Single harmonics. `http://principles.ou.edu/earth_figure_gravity/single_harmonics.jpg`, 2007.

[4] Thierry Appourchaux, K Belkacem, A-M Broomhall, WJ Chaplin, DO Gough, G Houdek, J Provost, F Baudin, P Boumier, Y Elsworth, et al. The quest for the solar g modes. *The Astronomy and Astrophysics Review*, 18(1-2):197–277, 2010.

[5] B Barbanis and L Woltjer. Orbits in spiral galaxies and the velocity dispersion of population i stars. *The Astrophysical Journal*, 150:461, 1967.

[6] Timothy R Bedding and Hans Kjeldsen. Solar-like oscillations. *Publications of the Astronomical Society of Australia*, 20(02):203–212, 2003.

[7] A. Blecha, G. Schaller, and A. Maeder. Fast pulsations in a Wolf-Rayet star. , 360:320, November 1992.

[8] A. P. Boss. Giant planet formation by gravitational instability. *Science*, 276:1836–1839, 1997.

[9] A. P. Boss. Stellar Metallicity and the Formation of Extrasolar Gas Giant Planets. , 567:L149–L153, March 2002.

[10] AP Boss. Gas giant protoplanets formed by disk instability in binary star systems. *The Astrophysical Journal*, 641(2):1148, 2006.

[11] Robert Hanbury Brown. The intensity interferometer: its application to astronomy. *Research supported by the Department of Scientific and Industrial Research, Australian Research Grants Committee, US Air Force, et al. London, Taylor and Francis, Ltd.; New York, Halsted Press, 1974. 199 p.*, 1, 1974.

[12] R Paul Butler, Geoffrey W Marcy, Eric Williams, Chris McCarthy, Preet Dosanjh, and Steven S Vogt. Attaining doppler precision of 3 ms. *Publications of the Astronomical Society of the Pacific*, pages 500–509, 1996.

[13] Kai Cai, Richard H Durisen, Scott Michael, Aaron C Boley, Annie C Mejía, Megan K Pickett, and Paola DAlessio. The effects of metallicity and grain size on gravitational instabilities in protoplanetary disks. *The Astrophysical Journal Letters*, 636(2):L149, 2006.

[14] WJ Chaplin, G Houdek, Christoffer Karoff, Y Elsworth, and R New. Mode lifetimes of stellar oscillations-implications for asteroseismology. *arXiv preprint arXiv:0905.1722*, 2009.

[15] J Christensen-Dalsgaard. What will asteroseismology teach us. In *Space Research in Stellar Activity and Variability*, volume 1, page 11, 1984.

[16] J Christensen-Dalsgaard. Some aspects of the theory of solar oscillations. *Geophysical & Astrophysical Fluid Dynamics*, 62(1-4):123–152, 1991.

[17] J Christensen-Dalsgaard and DO Gough. On the interpretation of five-minute oscillations in solar spectrum line shifts. *Monthly Notices of the Royal Astronomical Society*, 198:141–171, 1982.

[18] J Christensen-Dalsgaard and F Pérez Hernández. The phase function for stellar acoustic oscillations. i-theory. *Monthly Notices of the Royal Astronomical Society*, 257:62–88, 1992.

[19] Jorgen Christensen-Dalsgaard and Gabrielle Berthomieu. Theory of solar oscillations. *Solar interior and atmosphere*, 1:401–478, 1991.

[20] Jørgen Christensen-Dalsgaard and Søren Frandsen. Radiative transfer and solar oscillations. *Solar Physics*, 82(1-2):165–204, 1983.

[21] TG Cowling. The non-radial oscillations of polytropic stars. *Monthly Notices of the Royal Astronomical Society*, 101:367, 1941.

[22] Margarida S Cunha, Conny Aerts, Jørgen Christensen-Dalsgaard, A Baglin, L Bigot, TM Brown, C Catala, OL Creevey, A Domiciano De Souza, P Eggenberger, et al. Asteroseismology and interferometry. *The Astronomy and Astrophysics Review*, 14(3-4):217–360, 2007.

[23] JD do Nascimento Jr, C Charbonnel, A Lebre, P De Laverny, and JR De Medeiros. Lithium and rotation on the subgiant branch ii. theoretical analysis of observations. *arXiv preprint astro-ph/0003010*, 2000.

[24] T. L. Duvall, Jr. A dispersion law for solar oscillations. *Nature*, 300:242, November 1982.

[25] F Galland, AM Lagrange, S Udry, A Chelli, F Pepe, D Queloz, JL Beuzit, and M Mayor. Extrasolar planets and brown dwarfs around af type stars. i. performances of radial velocity measurements, first analyses of variations. *arXiv preprint astro-ph/0509111*, 2005.

[26] L Gizon and SK Solanki. Determining the inclination of the rotation axis of a sun-like star. *The Astrophysical Journal*, 589(2):1009, 2003.

[27] D. O. Gough. Asymptotic sound-speed inversions. In D. O. Gough, editor, *NATO ASIC Proc. 169: Seismology of the Sun and the Distant Stars*, pages 125–140, 1986.

[28] A. P. Hatzes, M. Zechmeister, J. Matthews, R. Kuschnig, G. A. H. Walker, M. Döllinger, D. B. Guenther, A. F. J. Moffat, S. M. Rucinski, D. Sasselov, and W. W. Weiss. The mass of the planet-hosting giant star β Geminorum determined from its p-mode oscillation spectrum. , 543:A98, July 2012.

[29] Artie P Hatzes and Mathias Zechmeister. The discovery of stellar oscillations in the planet-hosting giant star β geminorum. *The Astrophysical Journal Letters*, 670(1):L37, 2007.

[30] J. A. Johnson, T. D. Morton, and J. T. Wright. Retired a stars: The effect of stellar evolution on the mass estimates of subgiants. , 763:53, January 2013.

[31] John Asher Johnson, Kimberly M Aller, Andrew W Howard, and Justin R Crepp. Giant planet occurrence in the stellar mass-metallicity plane. *Publications of the Astronomical Society of the Pacific*, 122(894):905–915, 2010.

[32] John Asher Johnson, Brendan P Bowler, Andrew W Howard, Gregory W Henry, Geoffrey W Marcy, Howard Isaacson, John Michael Brewer, Debra A Fischer, Timothy D Morton, and Justin R Crepp. A hot jupiter orbiting the 1.7 m subgiant hd 102956. *The Astrophysical Journal Letters*, 721(2):L153, 2010.

[33] John Asher Johnson, R Paul Butler, Geoffrey W Marcy, Debra A Fischer, Steven S Vogt, Jason T Wright, and Kathryn MG Peek. A new planet around an m dwarf: revealing a correlation between exoplanets and stellar mass. *The Astrophysical Journal*, 670(1):833, 2007.

[34] John Asher Johnson, Geoffrey W Marcy, Debra A Fischer, Gregory Laughlin, R Paul Butler, Gregory W Henry, Jeff A Valenti, Eric B Ford, Steven S Vogt, and Jason T Wright. The n2k consortium. vi. doppler shifts without templates and three new short-period planets. *The Astrophysical Journal*, 647(1):600, 2006.

[35] John Asher Johnson, Geoffrey W Marcy, Debra A Fischer, Jason T Wright, Sabine Reffert, Julia M Kregenow, Peter KG Williams, and Kathryn MG Peek. Retired a stars and their companions. ii. jovian planets orbiting κ crb and hd 167042. *The Astrophysical Journal*, 675(1):784, 2008.

[36] Grant M Kennedy and Scott J Kenyon. Planet formation around stars of various masses: the snow line and the frequency of giant planets. *The Astrophysical Journal*, 673(1):502, 2008.

[37] R Kippenhahn and A Weigert. Stellar structure and evolution, 1990. *SpringerVerlag, Berlin, Germany.*

[38] H Kjeldsen and TR Bedding. Amplitudes of stellar oscillations: the implications for asteroseismology. *arXiv preprint astro-ph/9403015*, 1994.

[39] S Lafrasse, G Mella, D Bonneau, G Duvert, X Delfosse, and A Chelli. Jmmc stellar diameters catalogue-jsdc (lafrasse+, 2010). *VizieR Online Data Catalog*, 2300:0, 2010.

[40] Horace Lamb. *Hydrodynamics*. Cambridge university press, 1993.

[41] G. Lenain, R. Scuflaire, M.-A. Dupret, and A. Noels. The epsilon-mechanism in PMS and MS delta Scuti stars. *Communications in Asteroseismology*, 147:93–96, January 2006.

[42] James P Lloyd. " retired" planet hosts: Not so massive, maybe just portly after lunch. *The Astrophysical Journal Letters*, 739(2), 2011.

[43] Mia Lundkvist, Hans Kjeldsen, and V Silva Aguirre. Ame-asteroseismology made easy. estimating stellar properties by use of scaled models. *arXiv preprint arXiv:1404.2099*, 2014.

[44] Nils Mole, Andrea Kerekes, and Robert Erdélyi. Effects of random flows on the solar f mode: I. horizontal flow. In *Helioseismology, Asteroseismology, and MHD Connections*, pages 451–466. Springer, 2009.

[45] Michael Perryman. *The exoplanet handbook*. Cambridge University Press, 2011.

[46] NE Piskunov. Synth-a code for fast spectral synthesis. *Stellar magnetism*, 92:102, 1992.

[47] James B Pollack, Olenka Hubickyj, Peter Bodenheimer, Jack J Lissauer, Morris Podolak, and Yuval Greenzweig. Formation of the giant planets by concurrent accretion of solids and gas. *Icarus*, 124(1):62–85, 1996.

[48] Peter Reegen. Sigspec-i. frequency-and phase-resolved significance in fourier space. *arXiv preprint physics/0703160*, 2007.

[49] M Salaris and S Cassisi. Stellar models with the ml2 theory of convection. *arXiv preprint arXiv:0807.0863*, 2008.

[50] R Samadi, D Georgobiani, M-J Goupil, RF Stein, A Nordlund, et al. Excitation of solar-like oscillations across the hr diagram. *arXiv preprint astro-ph/0611762*, 2006.

[51] Bun'ei Sato, Masashi Omiya, Hiroki Harakawa, Hideyuki Izumiura, Eiji Kambe, Yoichi Takeda, Michitoshi Yoshida, Yoichi Itoh, Hiroyasu Ando, Eiichiro Kokubo, et al. Substellar companions to seven evolved intermediate-mass stars. *arXiv preprint arXiv:1207.3141*, 2012.

[52] Kevin C Schlaufman and Joshua N Winn. Evidence for the tidal destruction of hot jupiters by subgiant stars. *The Astrophysical Journal*, 772(2):143, 2013.

[53] KA Tah. Spectroscopy made easy tutorial. `http://exoplanets.astro.yale.edu/science/analysis/sme_tutorial.pdf`, Apr 2004.

[54] Neil James Tarrant. *Asteroseismology from the main sequence to giant stars.* PhD thesis, University of Birmingham, 2010.

[55] Edward W Thommes, Soko Matsumura, and Frederic A Rasio. Gas disks to gas giants: Simulating the birth of planetary systems. *Science*, 321(5890):814–817, 2008.

[56] JA Valenti and Nikolai Piskunov. Spectroscopy made easy: A new tool for fitting observations with synthetic spectra. *Astronomy and Astrophysics Supplement Series*, 118:595–603, 1996.

[57] Jeff A Valenti, Debra Fischer, Geoffrey W Marcy, John A Johnson, Gregory W Henry, Jason T Wright, Andrew W Howard, Matt Giguere, and Howard Isaacson. Two exoplanets discovered at keck observatory. *The Astrophysical Journal*, 702(2):989, 2009.

[58] Jeff A Valenti and Debra A Fischer. Spectroscopic properties of cool stars (spocs). i. 1040 f, g, and k dwarfs from keck, lick, and aat planet search programs. *The Astrophysical Journal Supplement Series*, 159(1):141, 2005.

[59] Floor Van Leeuwen. Validation of the new hipparcos reduction. *arXiv preprint arXiv:0708.1752*, 2007.

[60] SV Vorontsov. The inverse problem of helioseismology-the speed of sound in the solar interior. *Soviet Astronomy Letters*, 15:21, 1989.

[61] Timothy R White, Timothy R Bedding, Dennis Stello, Thierry Appourchaux, Jérôme Ballot, Othman Benomar, Alfio Bonanno, Anne-Marie Broomhall, Tiago L Campante, William J Chaplin, et al. Asteroseismic diagrams from a survey of solar-like oscillations with kepler. *The Astrophysical Journal Letters*, 742(1):L3, 2011.

[62] Jason T Wright, Onsi Fakhouri, Geoffrey W Marcy, Eunkyu Han, Ying Feng, John Asher Johnson, Andrew W Howard, Debra A Fischer, Jeff A Valenti, Jay Anderson, et al. The exoplanet orbit database. *Publications of the Astronomical Society of the Pacific*, 123(902):412–422, 2011.

[63] JT Wright. Radial velocity jitter in stars from the california and carnegie planet search at keck observatory1. *Publications of the Astronomical Society of the Pacific*, 117(833):657–664, 2005.

[64] S. K. Yi, Y.-C. Kim, and P. Demarque. The Y^2 Stellar Evolutionary Tracks. , 144:259–261, February 2003.